https://doi.org/10.1016/j.icarus.2022.115422

Geologic History of the South Circumpolar Region (SCR) of the Moon

Krasilnikov S.S.[1, 2*], Ivanov M.A.[1], Head J.W.[3], Krasilnikov A.S.[1]

1 - Vernadsky Institute of Geochemistry and Analytical Chemistry RAS, 119991 Moscow, Russia; 2 - Planetary Remote Sensing Laboratory, Department of Land Surveying & Geo-Informatics, The Hong Kong Polytechnic University, Hong Kong, PR China; 3 - Brown University, Providence RI, USA.

* Corresponding author at: The Hong Kong Polytechnic University (PolyU), 6/F, South Wing, PolyU Phase 8, 181 Chatham Road South, Hung Hom, Kowloon, Hong Kong, PR China.
E-mail address: sergey.krasilnikov@polyu.edu.hk (Krasilnikov S.S.).

Abstract

Space exploration missions have placed renewed focus on the South Circumpolar Region (SCR) of the Moon due to its unexplored nature by landed missions, potential water resources, proximity to the ancient South Pole-Aitken (SPA) basin, and the presence of regions that provide near-permanent solar illumination. Unlike previous surface exploration sites, the SCR lacks extensive mare regions and is most similar to the Apollo 16 and Luna 20 sites, and is dominated by overlapping deposits of impact craters and basins of a wide range of sizes and ages. This renders the geologic history of individual regions difficult to determine, and the provenance of returned samples potentially enigmatic. In order to help alleviate these problems and to provide a consistent geological framework for landing site selection, mission planning and operations, and interpreting sample provenance, we have compiled a new geologic map of the SCR (1:300 000 mapping scale; South pole to 70°S) using the most recently acquired orbital data (LRO LROC WAC 100 m/pix resolution image data and LOLA-based 80–20 m/pix resolution DTMs), and portraying geological units, features and structures, stratigraphic sequences, and providing a framework to address many outstanding problems in lunar science. We define and map several major types of units and structures: (1) high-standing massifs of the SPA basin, (2) crater-related units – walls, rims, and ejecta of impact craters and smaller basins, (3) plains units of both impact (impact melt and/or Cayley Formation) and volcanic origins (lava fields and pyroclastic deposits) and (4) landforms related to degradation of crater topography. Absolute Model Ages (AMAs) derived from crater size-frequency distribution (CSFD) measurements for ~200 of these units/structures, whose relative ages were determined by superposition relations, were used to compile a correlation of map units for the SCR region.

Keywords:

Moon, South pole, geology, geological mapping, landing site, SPA, WEH, Luna-25, Artemis

1. Introduction

The South Circumpolar Region (SCR) of the Moon is a destination of several future lander-oriented interplanetary missions. The Russian Luna-25 mission is targeted to land in a region between 65–75°S, 0–52°E (Djachkova et al., 2017; Ivanov et al., 2018a). NASA's VIPER (Volatiles Investigating Polar Exploration Rover) mission is declared as a beginning of a vast Artemis program aimed at building a human lunar base in the SCR (NASA, 2020). China National Space Administration (CNSA) missions Chang'e-6 and 7, ESA's mission EL3 (European Large Logistics Lander) and Indian Space Research Organisation (ISRO) mission Chandrayaan 3 are all oriented toward landing in the SCR of the Moon. All these missions require scientific and, in particular, geological support, that was recognized before implementing one of the most successful lunar exploration endeavors, the Apollo program (Wilhelms, 1974).

The enhanced scientific interest in the SCR is linked to its two key features. First is the increased concentration of hydrogen in the regolith (Mitrofanov et al., 2010, 2012; Boynton et al., 2012; Litvak et al., 2012; Sanin et al., 2012, 2017), which is interpreted to reflect the presence of ice in the subsurface (Mitrofanov et al., 2012). Second is the proximity of the SPA basin, which is the largest (Stuart-Alexander, 1978; Wilhelms et al., 1979; Wilhelms, 1987) and the oldest (Hiesinger et al., 2012) known lunar basin. Its ejecta certainly affected the SCR (Petro and Pieters, 2004, 2006; Melosh et al., 2017; Ivanov et al., 2018b; Moriarty et al., 2021) and delivered to the SCR the oldest materials of the lunar crust and perhaps mantle.

Geological maps are 2-dimensional representations of a 4-dimensional (X, Y, Z, time) geological space that portray the distribution of specific geological processes in space and time. Because of this, a geological map is an essential component of our understanding of fundamental problems of planetary geology. Geological maps also play a key role in the scientific support of interplanetary exploration missions because they allow task-oriented search, characterization, and selection of landing sites.

The quality and spatial resolution of available images determine the accuracy at which specific material/structural units and features can be defined and the scale at which these units are mapped. Until recently and aside from larger scale landing site maps (Bernhardt et al., 2022), only two original geological maps of the SCR of the Moon were available: 1) the geological map of the south side of the Moon that was compiled in 1979 at 1:5 000 000 scale (Wilhelms et al., 1979) and remastered using geographic information system (GIS) software in 2020 (Fortezzo et al., 2020), 2) the map of the SPA basin at 1:500 000 scale (Poehler et al., 2020). The map by Wilhelms represents the results of the photogeological analysis of the Moon's surface based on Lunar Orbiters IV and V images with a spatial resolution of around 225 m/pix (Kirk et al., 2008). The remastered map (Fortezzo et al., 2020) adopted geological units defined and mapped by Wilhelms et al. (1979) and presented them in GIS format. This provides the possibility to analyze material units with the help of the recently collected and higher-resolution datasets from various instruments on board recent and current missions (Ohtake et al., 2008; Robinson et al., 2010; Smith et al., 2010; Barker et al., 2016, 2021). The geological map of the SPA basin (Poehler et al., 2020) is based on images with higher resolution (the Lunar Reconnaissance Orbiter, LRO, Wide Angle Camera, WAC, 100 m/pix, and Narrow Angle Camera, NAC, 0.5–1.5 m/pix, Kaguya Terrane Camera, TC, ~10 m/pix) and was compiled at a more detailed scale. Our map partly overlaps with the southern part of the Poehler's et al. (2020) map and extends beyond the edges of SPA in this region.

2. Data and methods

We defined and mapped morphological units in the map region using the LROC WAC mosaic (100 m/pix resolution) and the LRO Lunar Orbiter Laser Altimeter (LOLA)-derived DTMs with a resolution of 20–80 m/pix. These data sets allow the compilation of a geological map at 1:300 000 scale using traditional geological mapping techniques (e.g., Wilhelms, 1972, 1987). The optical images are better suited for determining the albedo and finer-scale morphological characteristics of landforms on the surface and were used to define the map units. The altimetry data in many cases show contacts between the units more clearly and were used (along with the optical images) for outlining unit boundaries. In key areas, we used LROC NAC images with ~0.5–1 m/pix resolution to analyze the surface morphology and refine relative ages of units. The smallest recognizable features shown in the map are secondary craters from different primary craters, with diameters of about 0.5-1 km.

Spatial and temporal variations of the mineralogical and chemical characteristics and composition of surface units are essential additional information utilized in defining and interpreting units in the geological maps (e.g., Head et al., 1978). To obtain this information, we compared our map with data from the Clementine, Chandrayaan-1 (M^3) and Kaguya (Multiband imager) missions that have been previously collected and published (Pieters et al., 1994; Blewett et al., 1997; Lucey et al., 1994, 1998, 2000; Kramer et al., 2013; Lemelin et al., 2022).

In order to estimate AMAs (Absolute Model Ages) of our mapped units, we have performed measurements of crater size-frequency distribution (CSFD) (Neukum et al., 2001) of about 200 areas using mostly the high-resolution LOLA DTM in a shaded-relief mode. These data allow identification and mapping of craters from 100 m (at 20 m/pix DTM) in diameter and larger. For CSFD analyses, however, we selected craters larger than 300 m in diameter. These measurements were conducted in areas of intercrater plains and in the larger craters, the floors of which are partly or completely smooth/flat deposits. For these craters we have mapped smooth, flat plains associated with recent impact craters and observe no albedo or spectral properties that suggest maria or cryptomaria, we interpret these to be impact melt deposits associated with the crater. In many cases, such measurements provide robust AMA estimates and allow correlation of units mapped in different parts of the study area. Not all craters, however, have floors suitable for accurate CSFD measurements. For small craters and craters with rougher floors, CSFD measurements were conducted in the zone of contiguous ejecta near the outer crater rim. We fully acknowledge that the target properties can affect the CSFD measurement results and, thus, the AMA estimates (van der Bogert et al., 2017). From our AMA estimates, we excluded those that have errors larger than 10% of the mean value. All results of the AMA determinations for craters are shown in supplementary material, Table 1S ; in total, we obtained 94 AMA estimates of craters with errors smaller than 10%.

For craters that are located in the studied area or affect it by ejecta/secondaries we have compiled a crater catalogue (South crater catalog, see the Data Repository) that includes all craters recognizable in both the WAC images and LOLA DTM (557 craters) in a diameter range from 5 to 928 km (Fig. 1S, in supplementary materials). As we compiled the catalogue, we excluded craters that form clusters of secondary craters. Thus, we believe that the catalogue contains mostly primary impact structures. Each entry of the catalogue includes information on the location, age, and morphological state of a crater (see the Data Repository).

3. Topographic characteristics of the map area

The SPA basin impact event created significant topographic variations that still dominate the SCR of the Moon (Solomon et al., 1982; Garrick-Bethell and Zuber, 2009) (Fig. 1a). Our study area comprises the southeastern portions of the basin and includes specific domains of the floor, rim, and possible zone of contiguous ejecta (between ~125–265°E); the total topographic range is about 16 km (from ~ -9.1 to ~7 km). Despite the presence of the SPA basin and its transition from the floor to the rim domains, the hypsogram of the study area is unimodal (Fig. 1b). This means that there is no pronounced regional scarp-like feature that separates the floor and the rim of the basin in the map area and the transition between the floor and the rim of the basin is rather gradual (Fig. 1d). In contrast, the northern edge of SPA is characterized by sharp bimodality reflecting the presence of the regional scarp between the floor and the rim (Ivanov et al., 2018b).

The floor domain of the SPA basin in the study area has a mean elevation of -3.5 km (hereafter one sigma) with a range from ~-9 to ~2.4 km. The mean elevation of the floor outside the largest craters/basins is about -3±0.9 km.

The rim domain (Wilhelms et al., 1979, Garrick-Bethell and Zuber, 2009) is characterized by isolated, both flat-topped and peak-shaped high-standing massifs that may represent relicts of the SPA basin outer rim. Similar massifs occur along the northern portion of the SPA rim (Ivanov et al., 2018b; Walsh et al., 2022a). Although there are significant topographic variations along the proposed outer rims (from ~-4.5 to ~7 km), the mean elevation in this domain is ~0.5±1.7 km. The outer rim mapped by Wilhelms et al. (1979) was identified from optical images and was verified by topography data (Fig. 1c). From the southern side, the rim is marked by an abrupt drop of surface elevation (mean elevation at the base of the rim is about -1±0.8 km); from the north, the outer rim gradually merges with the SPA basin ejecta domain.

Beyond the SPA outer rim, there is interpreted to be a domain of the contiguous ejecta from the basin (Melosh et al., 2017; Moriarty et al., 2021). Topography in this domain is highly variable and if the largest craters are excluded, the mean elevation in this domain is ~0.7±~1.1 km. Such terrains in much younger basins, such as Orientale, provide important information about the thickness of rim ejecta (e.g., Fassett et al., 2011), but the surface in this domain in the ancient SPA basin has been reworked too intensely by impact structures larger than 100 km diameter, such as Bailly basin and craters Klaproth, Boussingault, Demonax, Moretus and Casatus, to make such estimates difficult (see also Guo et al., 2018).

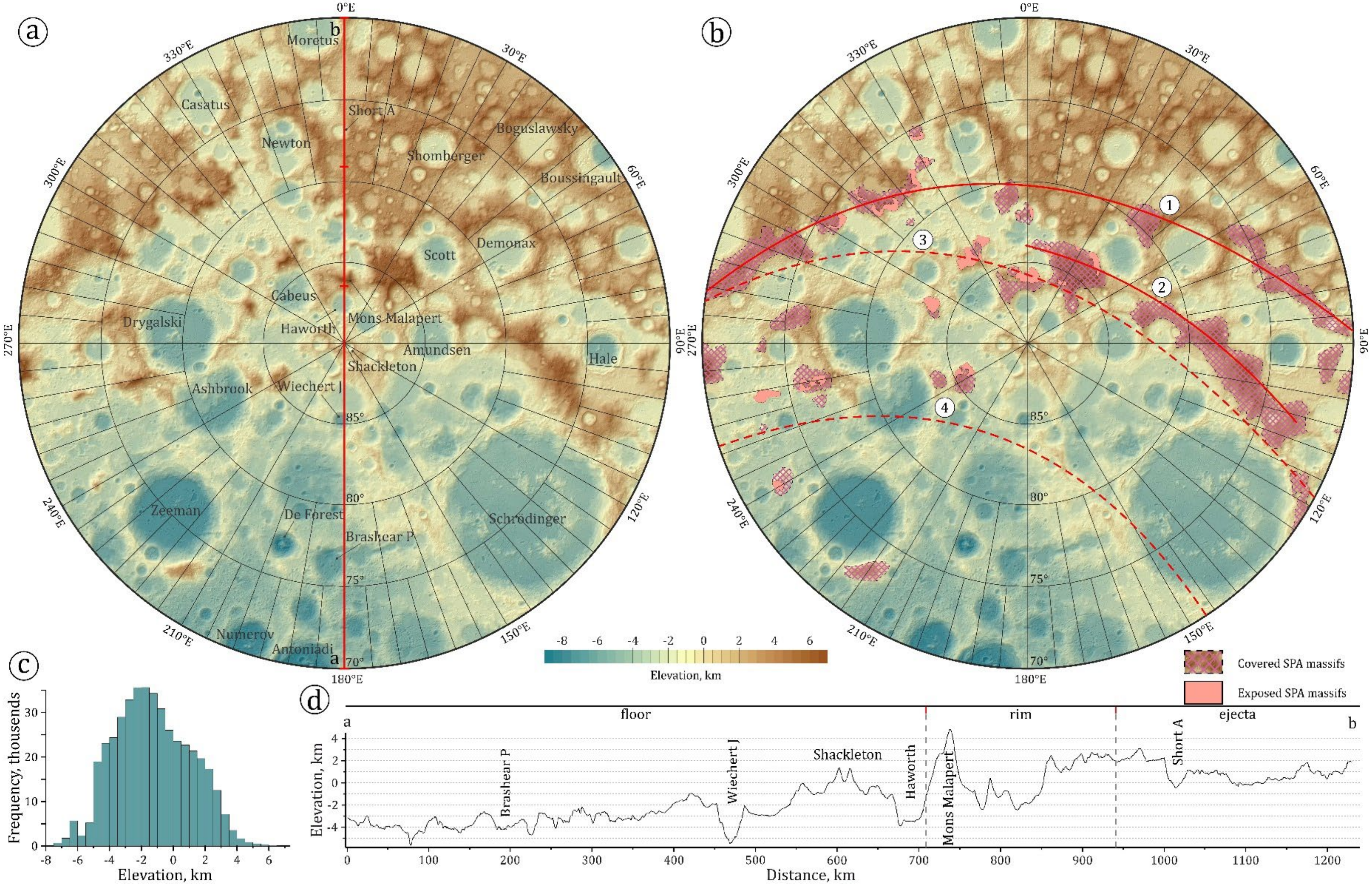

and to the area of possible contiguous ejecta (domains marked in the profile). (b) Locations of the rings of the SPA basin: (1) Outer ring (Wilhelms et al., 1979), (2) outer ellipse massifs correlated with the outer topographic ellipse (3), (4) best-fit topographic ellipse (Garrick-Bethell and Zuber, 2009). (c) Hypsogram of the studied area.

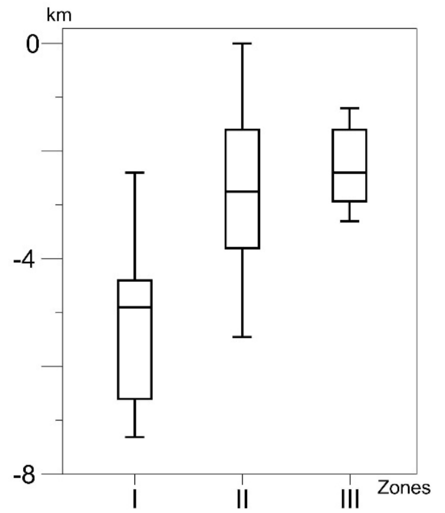

Fig. 2. Box plot of craters and basins floor elevation in the SPA domains: I – floor; II – rim; III – ejecta.

The outer and best-fit topographic ellipses of the SPA basin were defined by Garrick-Bethell and Zuber (2009) based on the topography of the basin and its iron and thorium signatures. The outer ellipse is correlated perfectly with the outer ellipse massif and isolated, high-standing massifs (Fig. 2c). The mean elevation of these ridges and massifs is ~2±1.7 km. The best-fit topographic ellipse is correlated with the lowland topography on the crater floor and spatial distribution of thorium and iron from the Lunar Prospector data (Garrick-Bethell and Zuber, 2009). Within this ellipse, the high-standing massifs are rare and isolated.

There are 20 large craters (>100 km) within the map area; their major topographic characteristics are summarized in Table 1. The depth to diameter ratios of these craters are comparable with the results reported in Pike (1976, 1977). In the table, the craters are divided into three groups depending upon their location relative to specific domains of the SPA basin. Fig. 22 shows that elevation of the floors of craters in the different SPA domains is controlled by the domain elevations. Floor domain (median: -4.9, quartiles: -4.4, -6.6); rim domain (median: -2.75, quartiles: -1.6, -3.8); ejecta domain (median: -2.4, quartiles: -1.6, -2.9).

Table 1. List of the largest (>100 km diameter) craters in the map area. Location and depth to diameter ratio.

Name	Lon., E	Lat., S	Diameter, D, km	Mean floor elevation (st.d.), km		Mean rim elevation (st.d.), km		Depth, d, km	d/D
Floor domain									
Amundsen-Ganswindt	124.6	81.5	379	-2.8	±0.4	0.3	±1.9	3.3	0.008
Schrödinger	133.1	74.7	313	-4.4	±0.3	-0.6	±1.1	6.2	0.012
Zeeman	224.4	75.1	185	-6.3	±0.1	-1.4	±1.1	5.5	0.027
Unnamed cr.	220.9	80.8	150	-4.4	±0.5	-3.4	±0.3	3.8	0.007
Antoniadi	187	69.4	137	-7.3	±0.01	-3.2	±0.5	4.8	0.03
Unnamed cr.	166.3	71	118	-4.8	±0.3	-2.7	±0.6	3.4	0.018
Numerov	197.4	70.6	111	-6.8	±0.2	-2.3	±0.7	4	0.041
Rim domain									
Unnamed cr.	109.1	68.6	252	-1.5	±0.2	0.8	±0.8	4.1	0.009
Unnamed cr.	87.7	75.3	175	-1.9	±0.3	1.8	±1	4.4	0.021
Drygalski	273.1	79.8	165	-4.6	±0.1	0.9	±0.7	7	0.033
Ashbrook	247.8	81.3	156	-5.4	±0.05	-0.4	±1.1	5.6	0.032
Unnamed cr.	97.1	73.7	124	-0.3	±0.3	1.8	±0.4	2.8	0.017
Demonax	59.3	78.5	120	-2.8	±0.08	1.9	±0.9	6.3	0.039
Le Gentil	284.4	74	120	-2.3	±0.2	1.1	±1.6	3.6	0.028
Cabeus	317.1	85.5	101	-3.4	±0.4	0.2	±1.2	6.2	0.036
Amundsen	86.4	84.6	100	-3.7	±0.07	0.6	±1.1	4.7	0.043
Ejecta domain									
Bailly	291.2	67.2	299	-1.4	±0.2	2.7	±1	5.6	0.014
Klaproth	332.3	70.2	130	-1.7	±0.1	0.6	±0.5	2.9	0.018

Boussingault	53.9	70.4	129	-	-	2.7	±0.7	-	-
Moretus	354	70.6	116	-3.2	±0.1	1.3	±0.6	6.1	0.039
Helmholtz	65.2	68.6	106	-2.9	±0.03	1.7	±0.4	5.2	0.043
Casatus	329	72.8	103	-2.4	±0.08	1.7	±0.8	5.2	0.04

4. Definition of map units

We defined units portrayed in the map area using standard geologic mapping procedures (e.g., Shoemaker and Hackman, 1962; Wilhelms, 1972) and practices, based primarily on their morphologic and topographic characteristics. Four types of landforms compose the surface in the map area.

(1) High-standing massifs of the SPA, (2) topographically contrasting features associated with craters (walls, rims, and ejecta of the smaller basins and craters), (3) level plains that mostly occur outside craters and can be of both impact (e.g., Cayley Formation; Oberbeck, 1975) and volcanic origin, (4) crater wall terraces and wall-floor arcuate lobes; we did not show terraces as a separate category and combined them together with crater walls.

4.1. High-standing massifs of the SPA

Topographically prominent massifs that are arranged along single trends likely represent pieces of rim and rings of the SPA basin. SPA basin outer rings cross the map area from the eastern side of Schrödinger basin, through the area at Mons Malapert to the eastern edge of the map area at ~280°E. The rims are heavily modified by subsequent impact events and appear as isolated high-standing massifs at 0.48±1.8 km, the most topographically prominent of which is Mons Malapert (Fig. 3) (e.g., Basilevsky et al., 2019). Figure 1 shows the spatial distribution of the remnants of the SPA rim crest and rings. These were identified based on two criteria: (1) massifs are isolated and unrelated to the rims of other craters and (2) a massif forms a prominence, i.e., the mean elevation of the summit area of an isolated massif is larger than the mean elevation of the immediate surroundings area plus one sigma. The massifs occur predominantly in the zone along the inferred rings of the SPA (Wilhelms et al., 1979; Garrick-Bethell and Zuber, 2009; Walsh et al., 2022a, b). Two massifs that satisfy the selection criteria are seen on the floor of SPA (Fig. 1c). We further divided the possible remnants of the SPA rings into categories of covered massifs (those overlapped by ejecta of neighboring craters, Fig. 1c) and exposed massifs (those lacking recognizable ejecta coatings and with steep slopes, Fig. 1c).

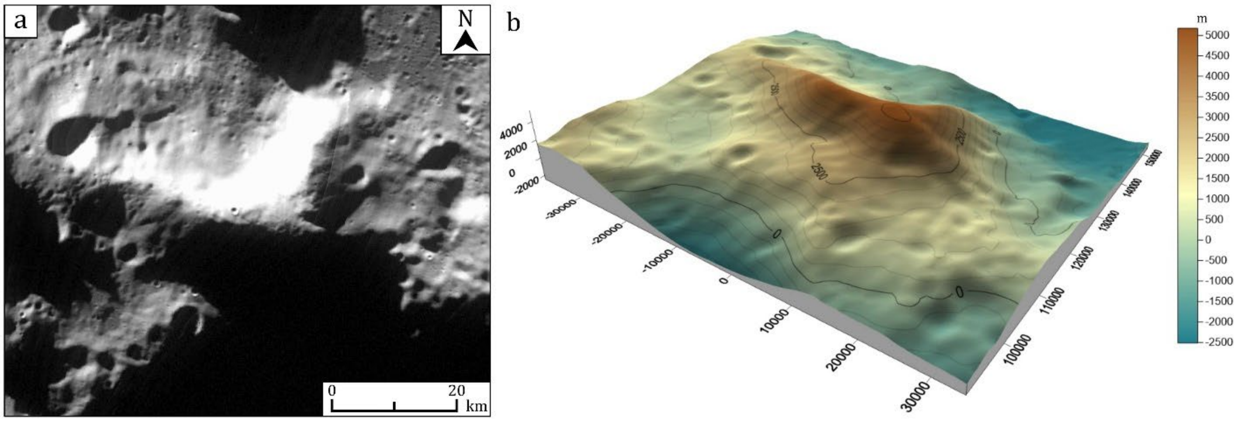

Fig. 3. (a) Morphology (portion of a LROC WAC mosaic) and (b) topography of Mons Malapert (LOLA DTM, contour lines are at 500 m; vertical exaggeration is 2x). Mons Malapert likely represents one of the most prominent exposures of the SPA basin rim.

4.2 Basins and crater materials

This type of landform includes central peaks and peak rings, crater walls, zones of contiguous ejecta, and fields/clusters of secondary craters. The central uplift/peak ring is an attribute of larger impact structures (Melosh, 1989; Baker et al., 2011) but sometimes significant central uplift is formed in smaller craters, for example, in Steinheim crater on Earth (~4 km diameter) (Ivanov and Stöffler, 2005). In the study region, the smallest crater with a central uplift is the crater Doerfel S, which is 29 km in diameter. According to Bernhardt et al., (2022) Shackleton has a hummocky floor that could partially be caused by central uplift. Peak ring formation usually characterizes larger craters/basins (> ~200 km diameter (Wilhelms, 1987; Baker et al, 2011); in the map area, the smallest crater with a peak ring is 137 km wide Antoniadi.

4.2.1 Basins

Besides the SPA basin, three officially recognized basins (impact structures >300 km diameter) occur in the map area (Spudis, 1993; Neumann et al., 2015). These are Schrödinger (75°S, 133°E, 313 km), Amundsen-Ganswindt (82°S, 125°E, ~380 km diameter) and Bailly (67°S, 291°E ~300 km) basins (Fig. 4). The study region is affected by secondary craters from the Orientale basin (e.g., Guo et al., 2018), although the parent basin is well beyond the map boundaries.

Subsequent impact craters strongly modify the floor domain of the SPA (e.g., craters Zeeman and Antoniadi, and the Schrödinger and Amundsen-Ganswindt basins) and the floor is largely overlain or influenced by their ejecta.

The rim domain of the SPA basin is punctuated by high-standing massifs that are best preserved along the outer topographic ellipse (Fig. 1c). In the area of the Schrödinger and Amundsen-Ganswindt basins, the massifs have been destroyed by those features and reappear again near crater Drygalski. In the floor domain, two individual massifs are seen near the crater Zeeman (Fig. 1c, 4); they may represent rim blocks that slid from the inner slope of the SPA basin.

The ejecta domain of the SPA basin is highly cratered and the surface has been intensely modified. However, a few massifs found in the ejecta domain may represent remnants of the original ejecta of the SPA. We used a method proposed by Fassett et al. (2011) to estimate the thickness of the basin ejecta in our study area. The model by Fassett et al. (2011) is based on measurements of craters that are semi-buried by ejecta from the Orientale basin. For the study area, the ejecta thickness values vary from ~2.5 km just beyond the outer SPA ring, to ~1 km at the greatest distance from the SPA edge of the map area near crater Moretus (Krasilnikov et al., 2023). These values suggest that craters larger than ~25 km in diameter were able to penetrate through the SPA ejecta deposit and may have excavated pre-SPA materials from beneath.

The heavily modified Amundsen-Ganswindt basin is currently expressed mostly as a topographic feature (Fig. 4). Only the southern portion of the basin is exposed, although subsequent impact events strongly degraded this area. Ejecta from the Schrödinger basin partly overlay and fill the interior of the Amundsen-Ganswindt basin.

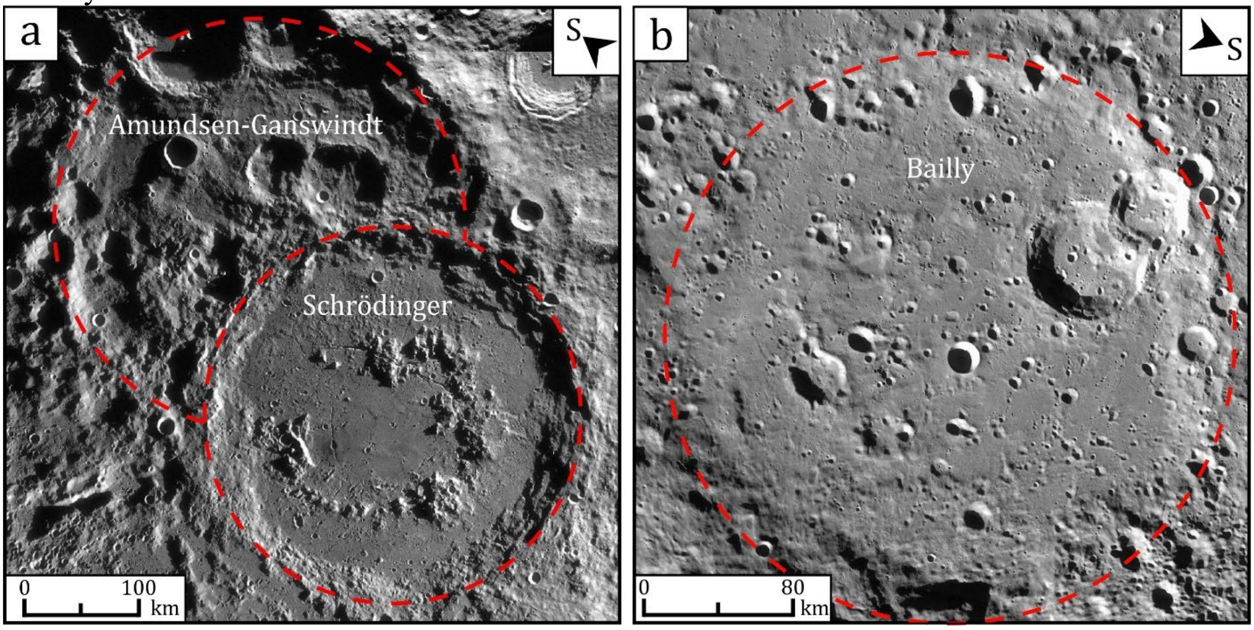

Fig. 4. Three officially recognized basins: a – Schrödinger and Amundsen-Ganswindt basins; b – Bailly basin, exist in the SCR mapped area, in addition to SPA.

Schrödinger is better preserved than Amundsen-Ganswindt (Fig. 4). It has a central peak ring surrounded by plains-like units. The plains are cut by grabens that may represent volcano-tectonic structures. The outer rim of the Schrödinger basin is prominent both topographically and morphologically. The rim is surrounded by contiguous ejecta and radiating from the rim area are three rimmed grabens formed by low-angle ejecta extend northward (~112ºE and ~130ºE, outside the map area) and eastward (~130ºE) from the basin rim.

Ejecta from the Orientale basin affected the study area and are represented by chains of secondary craters and areas of smooth plains (e.g., Guo et al., 2018), which have also been mapped elsewhere around the basin (Meyer et al., 2016). The thickness of such plains was estimated using the approach described by Fassett et al., (2011) and is smaller than ~ 30 meters (Krasilnikov et al., 2023) in the sector between 305–335ºE (Guo et al., 2018). A few craters (von Baeyer, de Forest P, Demonax A, -B, Newton E, Svedberg) are interpreted as secondary craters of the Orientale basin (Wilhelms et al., 1979).

4.2.2 Crater materials

We have divided craters in the study area into four categories according to their state of preservation (Head, 1975) and mapped specific components of the craters such as the floor, walls, rims, and ejecta as a single unit.

(1) The freshest craters are those that have a sharp rim crest and morphologically prominent zone of rough-textured contiguous ejecta and fine-scale radial grabens (Fig. 5a). In the SCR, we have mapped only one such crater – Schomberger A (~29 km diameter). In the hillshade image, this crater has a central peak surrounded by plains-forming materials (likely, impact melt). Ejecta materials stand out due to their high albedo (e.g., Bernhardt et al., 2022, Fig. 1A).

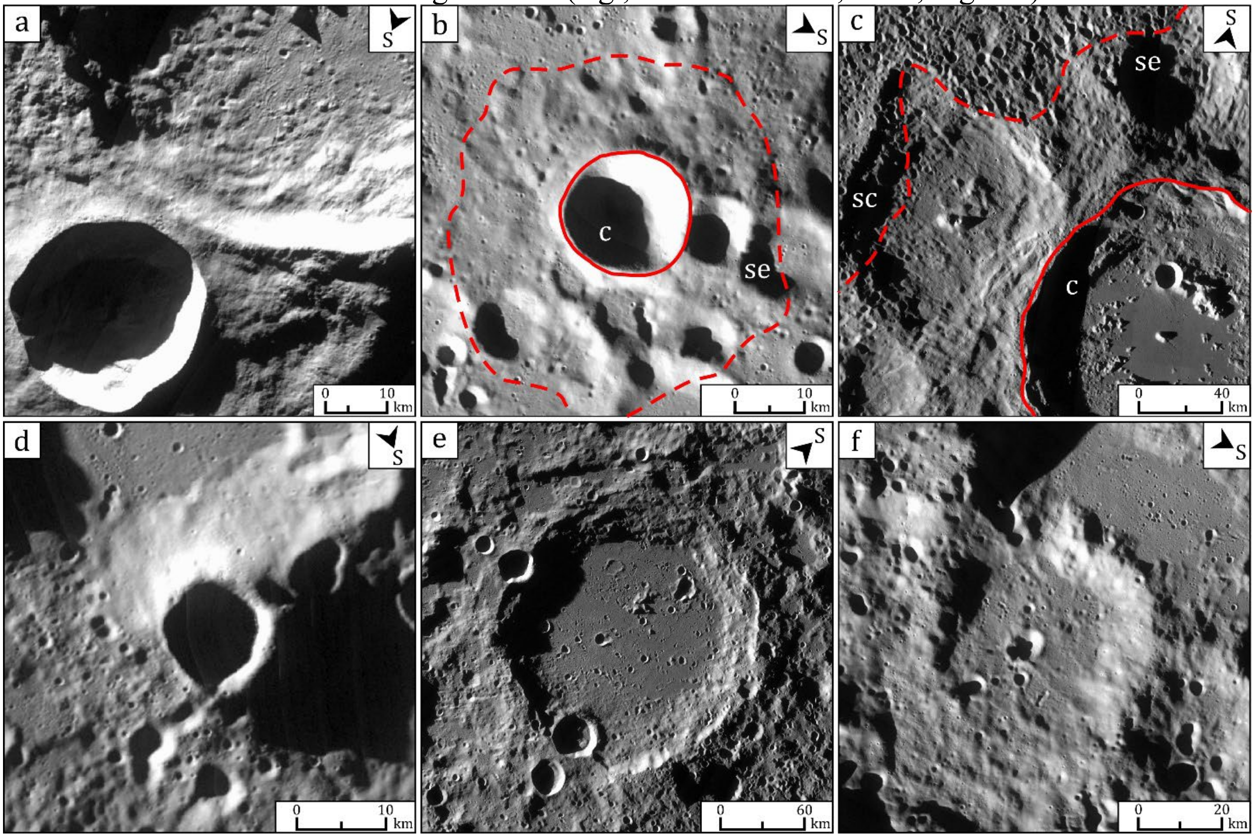

Fig. 5. Type localities of morphological categories of craters defined in our study (LROC WAC images): (a) craters with a sharp rim and prominent ejecta (an example: Schomberger A, 78.6ºS 23.5ºE); (b) craters with a sharp rim and distinguishable contiguous ejecta (se) (Le Gentil G, 71.7ºS 300.9ºE); (c, d) more degraded craters without extensive ejecta but with prominent fields of secondary craters (sc) for large craters (Antoniadi, 69.3ºS 186.9ºE) and small craters mainly without secondaries (Unnamed crater, 81.1ºS 338.3ºE); (e) highly degraded craters with prominent

rim and ejecta surrounding the rim crest (Zeeman, 75.1ºS 224.9ºE); (f) strongly degraded crater with morphologically and topographically subdued rims (Unnamed crater, 60.9ºS 282.7ºE).

(2) Craters with sharp rims and distinguishable contiguous ejecta. These craters are more abundant in the studied region (Fig. 5b). Usually, these are relatively small, bowl-shaped craters that do not exceed 20 km across with a mean diameter of 13±12 km. For the larger craters of this category, arcuate niches on the rim that likely reflect listric faults are typical. A good example of a small craters in this category is Wapowski crater (~11 km diameter), a crater type transitional from the previous smaller category. It has a bowl-shaped profile, sharp-crested rim and is surrounded by proximal ejecta. Larger craters, e.g. Hale Q (~23 km), typically have wall-floor arcuate lobes on the crater floor and distinguishable ejecta.

(3) Degraded craters are represented by structures with rounded rim crests. Larger craters of this category are surrounded by prominent fields of secondary craters (Fig. 5c) that begin just beyond the outer boundary of zones of contiguous ejecta. The sizes of these craters vary from 5 to 137 km, with a mean diameter of 17±20 km. Two craters in this category have a diameter of more than 100 km – Moretus (116 km) and Antoniadi (137 km). The floor of the larger craters is covered by plains-forming materials (likely to be impact melt) and the inner slopes of the rim (wall) are terraced. Small-sized craters in this category are typically bowl-shaped and have poorly recognizable ejecta (Fig. 5d).

(4) Subdued craters usually have a noticeable rim with a surrounding zone of contiguous ejecta, but both these components are subdued morphologically (Fig. 5e). No fields/chains of secondary craters are seen in association with these craters. This crater category is the most abundant in the map area; their diameters vary from 5 to 379 km, with a mean of 41±52 km. The larger craters of this category are topographically prominent with raised rims and the smaller degraded craters usually appear as rounded topographic lows (Fig. 5f). The subdued craters often coalesce and form rugged surfaces with abundant irregular hills and short, randomly oriented ridges that occur in some places of the study area.

4.3 Plains-forming units

Within the SCR map area, we have defined four varieties of plains-forming materials.

(1) Light plains that partly fill isolated craters or groups of craters (Fig. 6a). The light plains cover only 26,903 km^2 (2.2% of total area, Tab. 2). Occurrences of the plains usually have irregular outlines and can be localized both inside impact craters and in intercrater areas between them. The spatial distribution of the light plains suggests that they may represent deposits of fine-grained fractions of ejecta of remote craters and/or basins (Muehlberger et al., 1973; Head, 1974; Oberbeck, 1975; Meyer et al., 2016). In a similar manner, we interpret these materials as deposits of fine-grained ejecta from remote craters/basins (materials akin to the nearside Cayley Formation; Wilhelms, 1987).

(2) Light-toned plains that partly cover the central portion of the floor of craters > ~30 km diameter and embay structures on the floor periphery (Fig. 6b). The plains have higher albedo and are likely to represent solidified pools of impact melt (Dhingra et al., 2017). Total area: 42,485 km^2 (3.5% of total area, Tab. 2).

(3) Plains that are localized on the floor of Schrödinger basin (Fig. 7, Ilv1) and Antoniadi crater have a smooth surface texture and low albedo. Furthermore, Kaguya data show enhanced abundanceies of FeO and high-Ca pyroxene (Lemelin et al., 2022) that correspond to these plains and dark plains (characterized below). These characteristics suggest that the plains are of volcanic origin (Kramer et al., 2013; Wilhelms, 1972). Materials of the plains fill the basin floor within its peak ring, and the surface of the plains shows several local graben, possibly related to a gradual filling of the floor from the different volcanic sources. Total area: 8,759 km^2 (0.7% of total area, Tab. 2).

(4) Darker plains with diffuse boundaries that are localized in the Schrödinger basin in close spatial association with the dark smooth plains (Fig. 7). Occurrences of the mantling deposits are also spatially associated with graben or fissures on the floor of the basin (Fig. 7, gr) and have been

interpreted as pyroclastic deposits (Kramer et al., 2013). The most extensive dark mantling deposit (Fig 7, Ipx2) surrounds a pear-shaped pit called Schrödinger G (~ 6 km diameter, a volcanic vent?) that is on top of a mound ~30 km across and ~ 400 m high. This feature was interpreted as the main center of pyroclastic activity within the Schrödinger basin (Kramer et al., 2013). Total area: 2,458 km^2 (0.2% of total area, Tab. 2).

A system of linear depressions (interpreted as graben) on the floor of the Schrödinger basin is in close spatial and genetic association with the volcanic landforms on the floor. The graben, thus, are interpreted to represent the surface manifestations of sill intrusions and the ascent of magmatic dikes (Schultz, 1976, 1977, 1978; Jozwiak et al., 2012; Head and Wilson, 2017; Wilson and Head, 2018). Besides the Schrödinger basin, there are two craters with fractured floors in the study area: an unnamed crater at ~356.4ºE, 82.8°S (33 km) and Moretus (70.6ºS 354ºE, 116 km, Fig. 5b). The floors of these craters show no signs of volcanic activity in the form of rimless, vent-like depressions and/or dark mantling. On the floor of Schrödinger basin wrinkle ridges (e.g. Lu et al., 2019) indicate tectonic forms caused by volcanic activity.

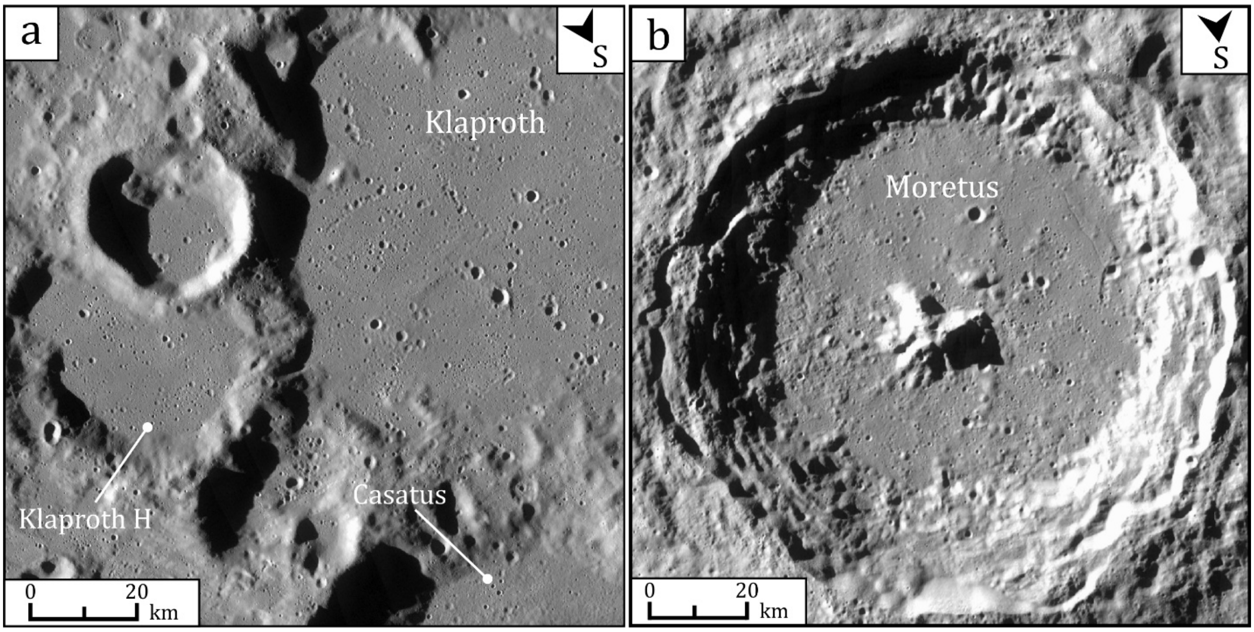

Fig. 6. (a) Interiors of crater Klaproth (right crater at image a) and smaller craters nearby are filled by plains with higher albedo, which may be akin to the nearside Cayley Formation. (b) The floor of Moretus crater covered by solidified impact melt material.

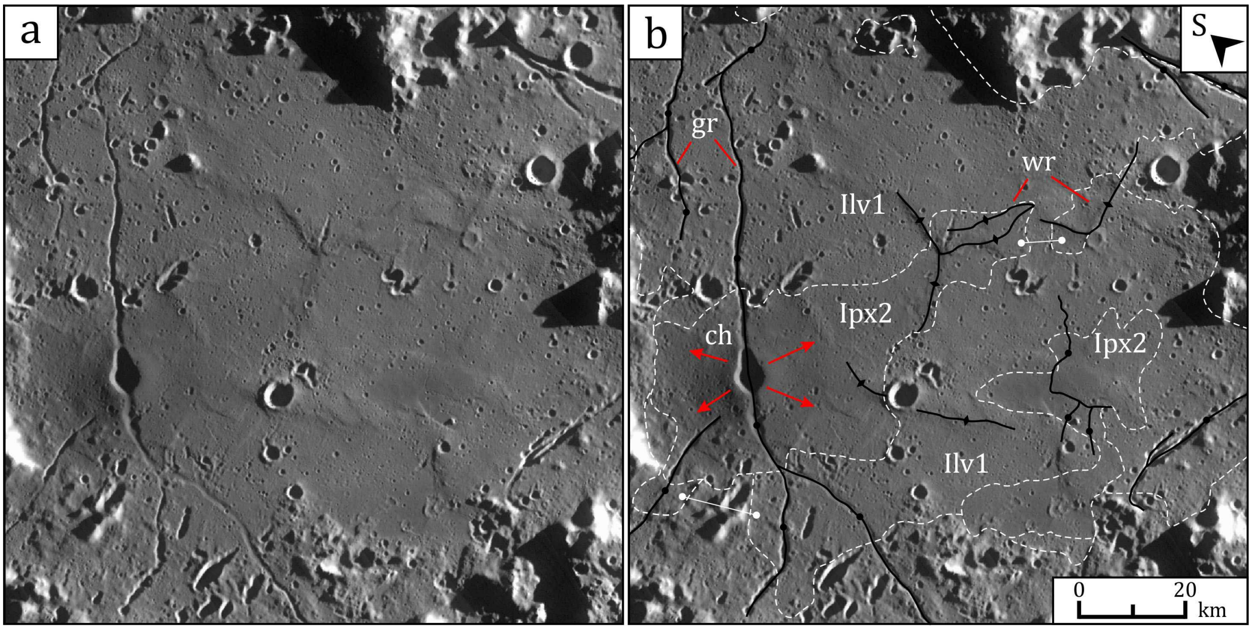

Fig. 7. (a) plains of volcanic origin on the floor of the Schrödinger basin inside its peak ring. (b) Ilv1 – lava plains, Ipx2 – dark mantling material of possible pyroclastic origin; ch – a low dome-like feature with a large summit depression that is thought to be the source of pyroclastic materials (Schrödinger G); gr – graben depressions (black line with circles); wr - wrinkle ridges (black line with rhombus).

4.4 Crater wall terraces/wall-floor arcuate lobes

In our study, we distinguish crater wall terraces for large craters (Fig. 8b) and wall-floor arcuate lobes typical for smaller craters (Fig. 8a).

Linear, parallel step-like terrace structures (Fig. 8b), often tilted toward the crater wall, occur between the crater rim crest and crater floor. These typically define several linear segments of the crater wall that form a polygonal pattern to the rim crest–commonly observed in complex craters (>~25 km diameter) and small basins (Pike, 1976). The mean diameter of craters/basins with wall terraces is 108±59 km. The surface manifestations of listric faulting are associated with crater central uplift and crater rim crest-wall collapse in the terminal stages of the impact event (Melosh, 1989). We included the wall terraces in the crater material units and did not map them separately.

Wall-floor arcuate lobes (Fig. 8a) may have been formed due to listric wall failure and represent wall collapse landforms. These occur predominantly in simple to complex transitional craters <~25 km diameter. These features are typical for craters with a mean diameter of 20±8 km. These are interpreted to represent the surface manifestation of listric faulting accompanying partial floor uplift and wall collapse in the terminal stages of impact crater formation in the simple-complex crater transition.

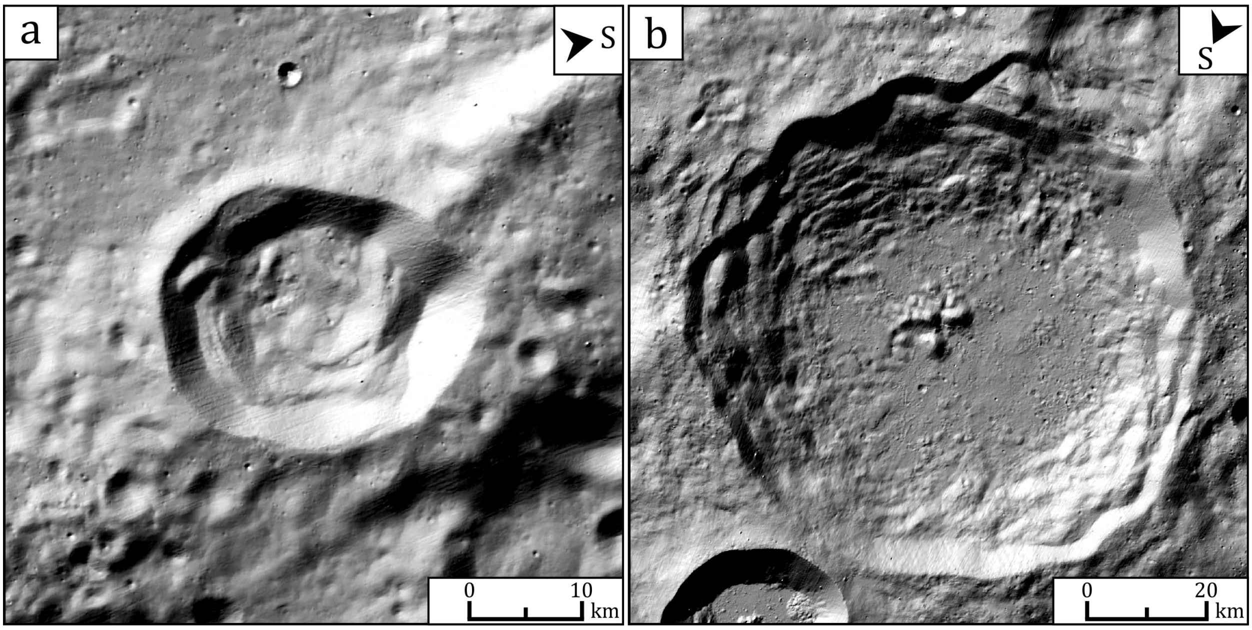

Fig. 8. Examples of crater wall terraces and wall-floor arcuate lobes in impact craters. a) Wall-floor arcuate lobes in crater Drygalski P (80.96ºS 260.25ºE). b) Crater wall terraces of crater Schomberger (76.67ºS 24.53ºE). Both images are hillshade representations of the LOLA DTM (resolution 60 m/pix).

4.5 Lobate scarps

More than 3200 lobate scarps on the Moon were identified and mapped (Watters et al., 2015). Lobate scarps in the study area occur in four localities as features less than ~35 km long. They were found on the outer rim of Simpelius crater (73.9ºS 10.1ºE), at the intercrater plain nearby Ibn Bajja crater (83.4ºS 273.3ºE), at the border of Cabeus A crater (82.1ºS 316.3ºE) and the floor of Newton crater (77.4ºS 344.6ºE) (Fig. 9b). These ridges may represent the youngest tectonic activity of the lunar crust (Lu et al., 2019; Watters et al., 2015) and may present seismic hazards for exploration missions (Mishra and Kumar, 2022). The main trend of the scarps is a northeast-southwest direction (Fig. 9a).

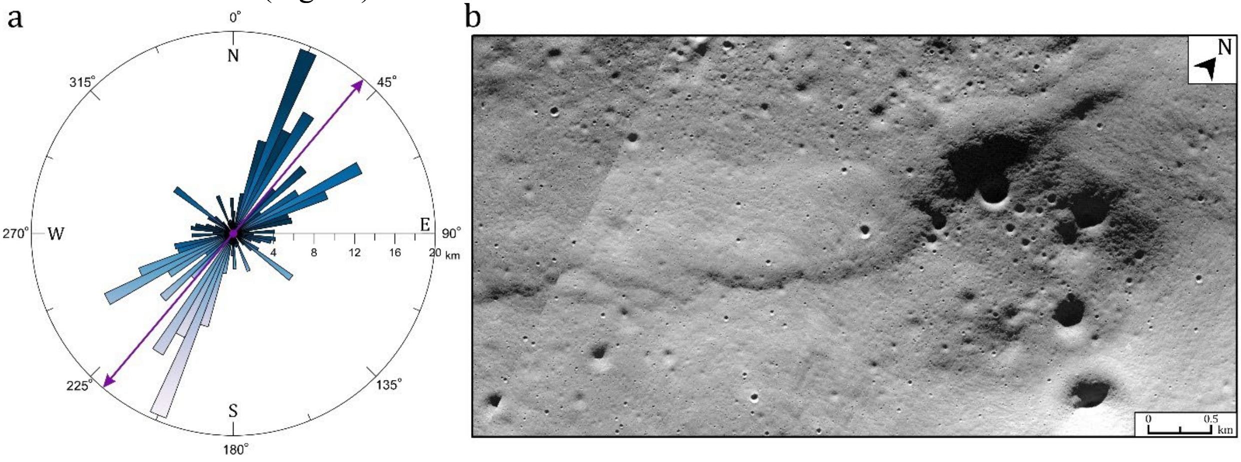

Fig. 9. a – polar bar chart illustrating the main trends of scarps. The size of sections describes the length of scarps per degree. The arrow shows the mean direction of the scarps in the SCR. b – example of a tectonic scarp shown in a NAC image, located on the floor of Newton crater.

5. Relative and absolute model ages of the map units

After the definition of the map units and their portrayal in a geomorphological map (Fig. 13), our next step was to determine the relative and absolute model ages of units, thereby transforming our geomorphological map into a geological map. The relative ages were established by superposition and crosscutting relationships (Shoemaker and Hackman, 1962; Wilhelms et al., 1979) and the AMAs were derived from numerous (~100) CSFD measurements.

The time-calibrated lunar stratigraphy applied in our work is based on the cratering chronology of Stöffler et al., (2006) and previous research referenced in this paper. Thus, the pre-Nectarian System is the oldest system of the Moon between its origin, dated as 4.52 Gyr (Lee et al., 1997; Halliday, 2000), and the formation of the Nectaris basin, which is probably ~3.92 Gyr old. The Imbrian impact basin marks the border between the Nectarian System and the Lower Imbrian Series at 3.85±0.02 Gyr. The boundary between the Lower Imbrian and Upper Imbrian Series, 3.75±0.01 Gyr, is defined by the absolute ages of basalt samples in the Apollo 17 landing site. The border between the Upper Imbrian Series and the Eratosthenian System is based on the dating of basalt samples in the Apollo 12 landing site. The age of Copernicus crater, 0.8±0.15 Gyr, marks the beginning of the Copernican System, based on analysis of units associated with this crater, and an analysis of material from this crater found at the Apollo 12 landing site.

The distinguishable morphology, prominent ejecta, and secondary craters indicate that craters possessing these features are the youngest in the study region. Features related to such primary craters overlay or cut all other adjacent landforms (Fig. 5a) and usually are considered to belong to the Copernican System (Wilhelms and McCauley, 1971; Wilhelms and El-Baz, 1977; Lucchitta, 1978; Wilhelms et al., 1979). The AMA of crater Schomberger A (78.6ºS 23.6ºE, 29 km diameter) is estimated to be 0.404±0.05 Ga (Copernican System, Fig. 10a).

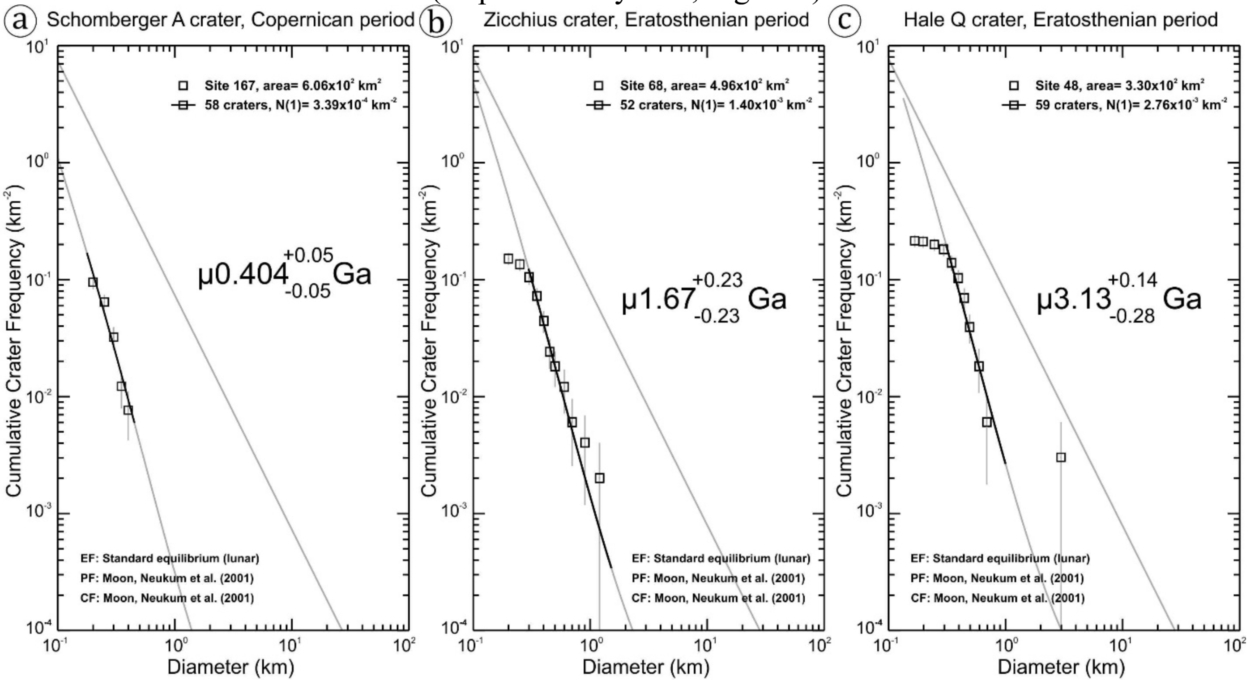

Fig. 10. Size-frequency distribution of primary craters superposed on the ejecta of Copernican (a) and Eratosthenian craters (b, c).

The AMAs of some other craters with sharp rims and morphologically distinguishable ejecta are estimated as 1.67±0.23 Ga (crater Zucchius, 61.4ºS 309.4ºE, 63 km diameter, Eratosthenian system, Fig. 10b) and 3.13 +0.14/-0.28 Ga (crater Hale Q, 76.5ºS 83.9ºE, 23 km diameter, Eratosthenian system, Fig, 10c).

We consider craters that are superposed by materials of Copernican and Eratosthenian craters, but have sharp rims and are surrounded by prominent fields of secondary craters, as Imbrian-aged craters (see Head, 1975). In our study, we have divided Imbrian craters between the Lower and Upper Imbrian Series according to their relationships with the stratigraphic marker provided by secondary craters from the Orientale basin that form chains of craters of about same size that are oriented toward Orientale basin was adopted as 3.72–3.77 Ga, following Stöffler and Ryder, (2001) (see also, discussion in Whitten et al., 2011)

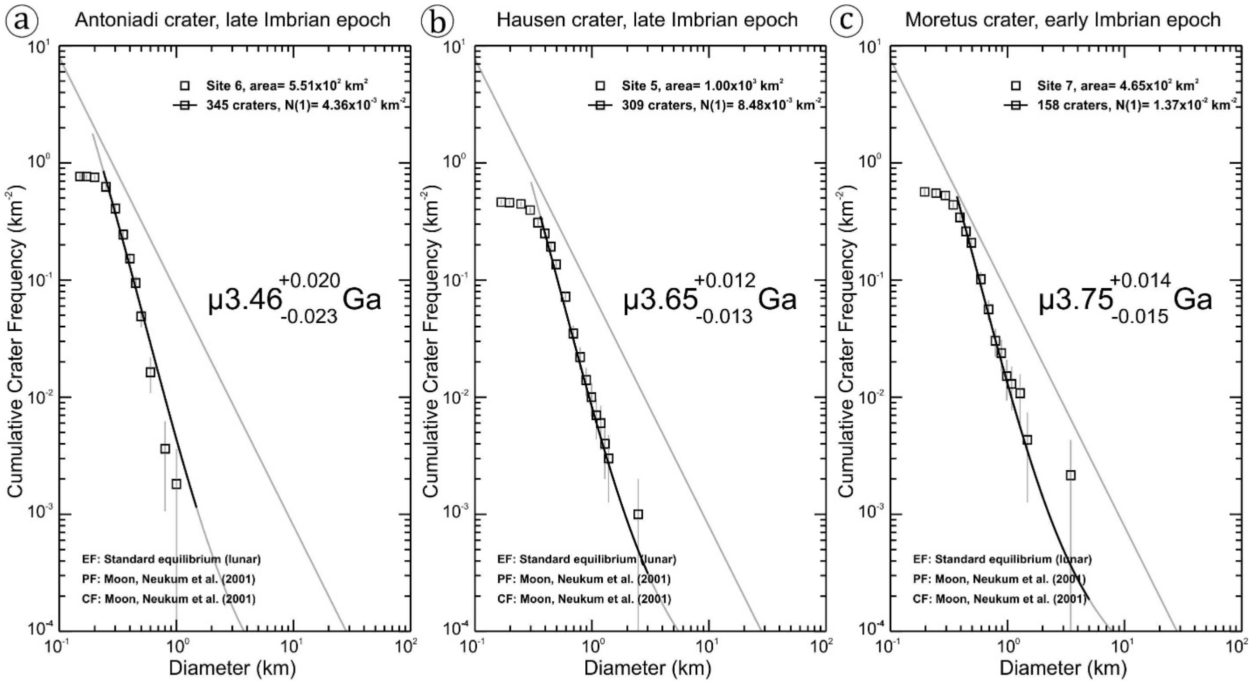

Fig. 11. Size-frequency distribution of superposed primary craters on the floor of Late (a, b) and Early Imbrian craters (c).

In the map area, we have found 77 craters belonging to the Upper Imbrian series and 37 craters to the Lower Imbrian Series. The larger Lower Imbrian craters on the floor of which we conducted CSFD measurements are Fizeau (58.2ºS 226.1ºE, 108 km) and Moretus (70.6ºS 354ºE, 116 km); their AMAs are 3.84 +0.034/-0.044 Ga and 3.75 +0.014/-0.015 Ga, respectively (Fig. 11c). The largest Upper Imbrian craters are Antoniadi (69.4ºS 187ºE, 137 km) and Hausen (88.8ºS 294.7ºE, 170 km) the AMAs for these are 3.46 +0.020/-0.023 Ga and 3.65 +0.012/-0.013 Ga, respectively (Fig. 11 a, b).

Nectarian craters are usually highly degraded and lack surrounding fields/chains of secondary craters. However, they have prominent rims with rounded crests and zones of contiguous ejecta surrounding the rim crests (Fig. 5e). In the map area, 50 craters and the Schrödinger basin were determined as Nectarian-aged structures and in the largest examples (nine structures) we were able to conduct CSDF measurements. The largest Nectarian impact features in the map area are: Schrödinger basin (74.7ºS 133.1ºE, 313 km, 3.89 +0.029/-0.036 Ga, Fig. 12a); Drygalski (79.8ºS 273.1ºE, 165 km, 3.93 +0.0095/-0.01 Ga); Demonax (78.5ºS 59.3ºE, 120 km); and Amundsen (84.6ºS 86.4ºE, 100 km, Fig. 12b). The morphology and stratigraphic relationships of crater Zeeman (75.1ºS 174.8ºE, 185 km) suggest that it is a Nectarian crater, but CSFD measurements on its floor yield an Imbrian age because the floor of Zeeman is overlapped by Imbrian-aged ejecta from Antoniadi and Zeeman E craters.

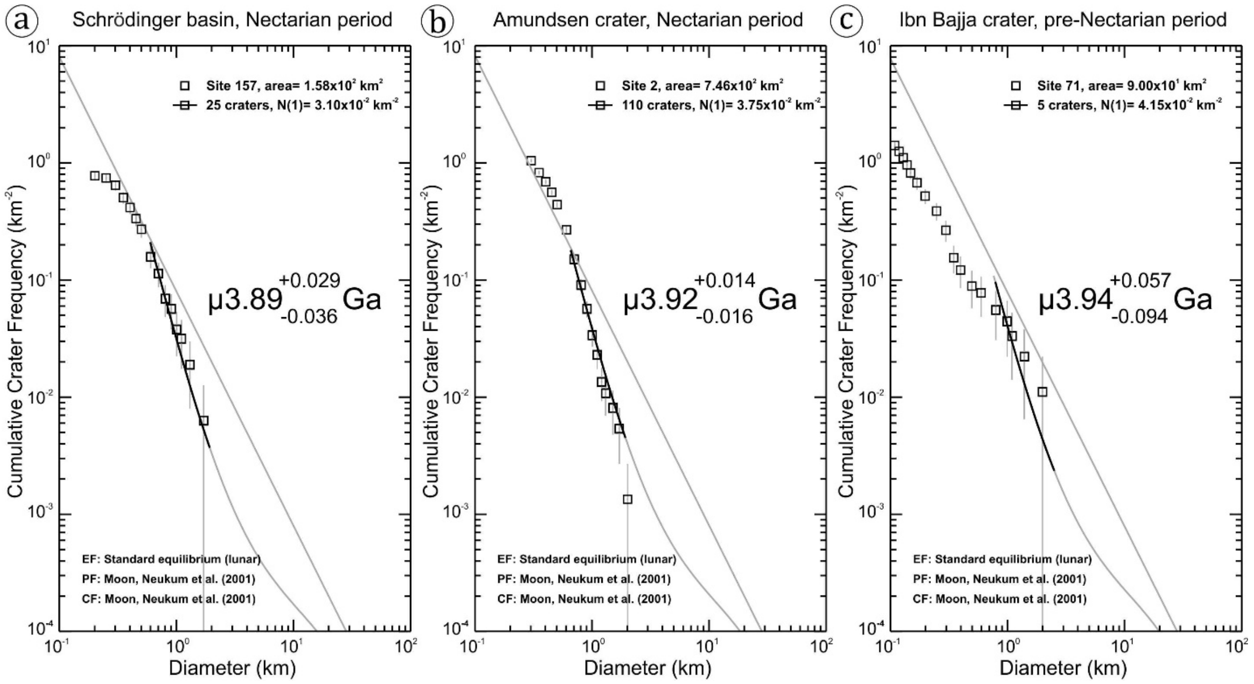

Fig. 12. Size-frequency distribution of superposed primary craters on the floor of Nectarian (a, b) and pre-Nectarian (c) impact structures. The CSFD measurements on the floor of Schrödinger basin were performed for the impact melt unit.

The subdued craters that show only parts of their rims along with the hummocky/rugged terrains (remnants of ancient craters) and the high-standing massifs (likely to be portions of the SPA basin rim and rings) collectively have been considered as pre-Nectarian features. 118 craters and one basin, Amundsen-Ganswindt (379 km), in the map area were considered as the pre-Nectarian structures. Among these, only two pre-Nectarian craters provide large enough areas on their floors where reliable CSFD measurements can be conducted: Ibn Bajja (86.3ºS 284.9ºE, 13 km, 4.02 +0.079/-0.19 Ga, Fig. 12c) and an unnamed crater at 82.3ºS 11.2ºE (30 km, 3.99 +0.041/-0.058 Ga).

Determination of the relative and absolute model ages of specific units in the study region allows the transformation of the initial geomorphological map into a geological map (Fig. 13), which is accompanied by a correlation chart and description of map units.

Table. 2. Exposed areas of map units (Fig. 2S).

System/Series	Origin and types of units	Units	Area, km^2	Area, %
Copernican	Impact structures	Cu, Cc, Cse, Csc	16,760	1.4
	Light-toned plains in larger craters	Cmrp	142	0.01
Eratosthenian	Impact structures	Ec, Ese, Esc, Ecl	24,537	2
Upper Imbrian	Impact structures	Icu2, Ic2, Ise2, Isc2, Icl2,	441,677	36.7
	Light-toned plains in larger craters	Imrp2, Imsp2	1,317	0.1
	Light plains	Ilp2	5,104	0.4
	Dark sharp plains	Ipx2	2,458	0.2
	Dark diffuse plains	Ilv2	194	0.02
Lower Imbrian	Impact structures	Icu1, Ic1, Ise1, Isc1, Icl1	94,013	7.8
	Basin material	Ioc	55,029	4.6
	Light-toned plains in larger craters	Imrp1, Imsp1	3,347	0.3
	Light plains	Ilp1	8,414	0.7
	Dark diffuse plains	Ilv1	8,565	0.7
Nectarian	Impact structures	Ncu, Nc, Nse, Nsc, Ncl	279,442	23.2
	Light-toned plains in larger craters	Nmrp, Nmsp	37,679	3.1

	Light plains	Nlp	7,895	0.7
pre-Nectarian	Impact structures	pNcu, pNc, pNse	109,059	9.1
	Basin material	pNbm	92,712	7.7
	South Pole-Aitken basin	SPA	8,731	0.7
	Light plains	pNlp	100	0.01
undivided age	Secondary craters	sc	2,430	0.2
	Light plains	lp	5,390	0.4
			1,199,891	100

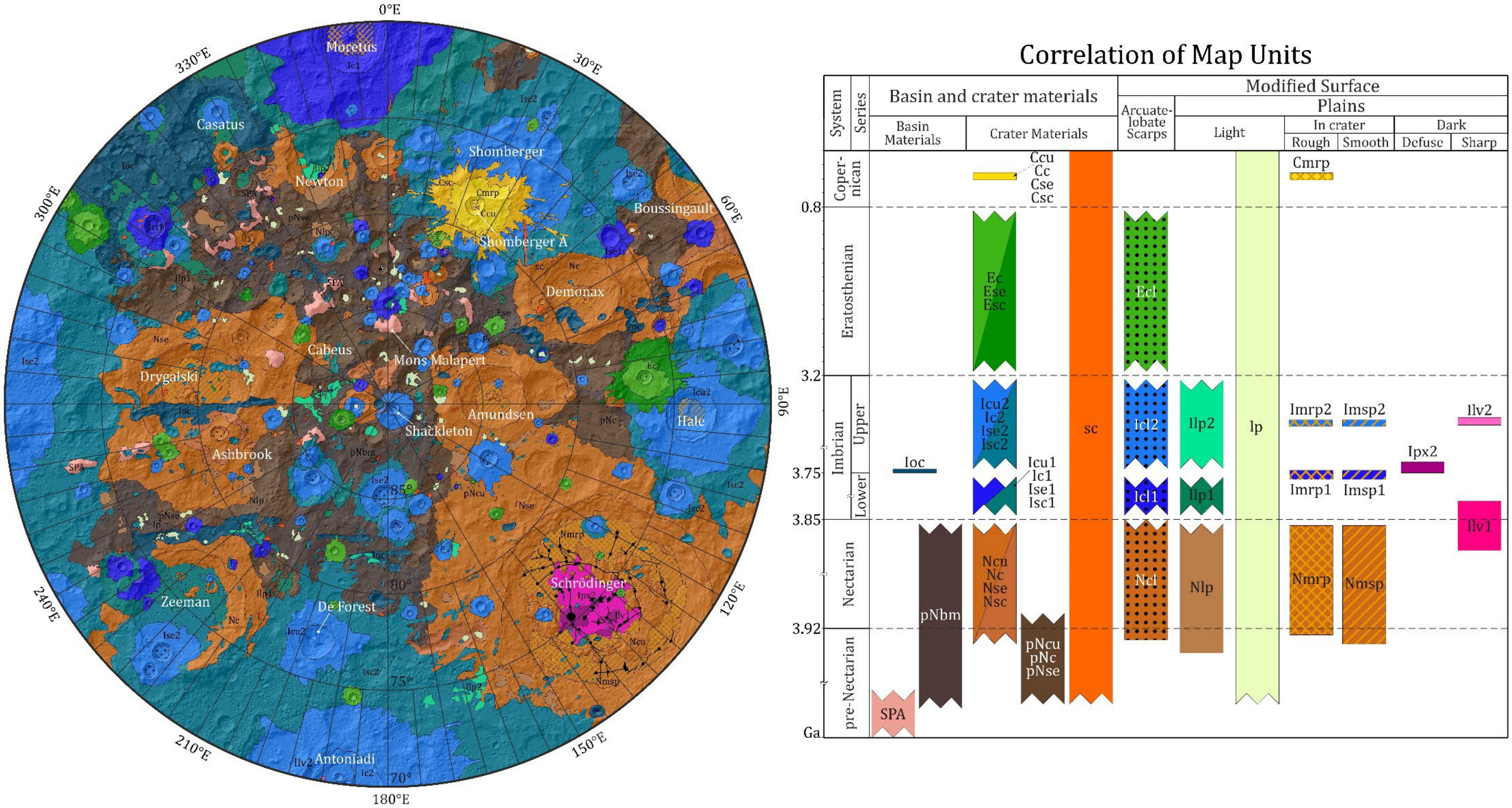

Fig. 13. Geological map of the South Pole region and correlation of the map units. Units divided by age shown in supplementary material Fig. 2S.

Description of Map Units

Materials of Primary Impact Craters and Their Secondary Craters

Copernican Crater Materials

Ccu	Ccu - CENTRAL PEAK in crater Schomberger A
Cc	Cc - CRATER INTERIORS. Floor and inner walls of crater Schomberger A
Cse	Cse - EJECTED MATERIAL from crater. Rough-textured contiguous ejecta of crater Schomberger A
Csc	Csc - EJECTED MATERIAL, SATELLITIC AND SECONDARY CRATERS of crater Schomberger A

Eratosthenian Crater Materials

Ec	Ec - CRATER INTERIORS. Interiors of sharp-crested, bowl-shaped craters; interpreted as Eratosthenian in age
Ese	Ese - EJECTED MATERIAL. Contiguous ejecta with subdued morphology at Eratosthenian craters
Esc	Esc - EJECTED, SATELLITIC AND SECONDARY CRATERS of Eratosthenian craters
Ecl	Ecl - CRATER ARCUATE-LOBATE SCARPS. Lobate scarps inside some Eratosthenian craters. *Interpretation:* materials of landslide formed by surface manifestation of listric faulting

Upper Imbrian Crater Materials

Icu2	Icu2 - CENTRAL PEAK AND PEAK RING of flat-floored large craters
Ic2	Ic2 - CRATER INTERIORS. Floor and inner terraced rim for large craters, or sharp rim and typically bowl shape for small-size craters; interpreted as Upper Imbrian age based on correlation of the absolute model ages and morphology
Ise2	Ise2 - EJECTED MATERIAL. Contiguous ejecta of Upper Imbrian craters
Isc2	Isc2 - EJECTED, SATELLITIC AND SECONDARY CRATERS of Upper Imbrian craters, mainly for large craters
Icl2	Icl2 - CRATER ARCUATE-LOBATE SCARPS. Lobate scarps inside some Upper Imbrian craters. *Interpretation:* materials of slumps/landslides formed by surface manifestation of listric faulting

Lower Imbrian Crater Materials

Icu1	Icu1 - CENTRAL PEAK in crater Moretus
Ic1	Ic1 - CRATER INTERIORS Floor and inner terraced rim or bowl-shaped interiors of Lower Imbrian craters; interpreted as Lower Imbrian age based on correlation of the absolute model ages and morphology
Ise1	Ise1 - EJECTED MATERIAL. Contiguous ejecta of Lower Imbrian craters
Isc1	Isc1 - EJECTED, SATELLITIC AND SECONDARY CRATERS of Lower Imbrian craters, typical for large craters
Icl1	Icl1 - CRATER ARCUATE-LOBATE SCARPS. Lobate scarps inside some Lower Imbrian craters. *Interpretation:* materials of slumps/landslides formed by surface manifestation of listric faulting

Nectarian Crater Materials

Ncu	Ncu - CENTRAL PEAK AND PEAK RING of flat-floored large craters
Nc	Nc - CRATER INTERIORS. Floor and inner terraced rim of flat-floored craters; interpreted as Nectarian in age based on correlation of the absolute model ages and morphology
Nse	Nse - EJECTED MATERIAL. Contiguous ejecta of Nectarian craters
Nsc	Nsc - EJECTED, SATELLITIC AND SECONDARY CRATERS of Nectarian craters
Ncl	Ncl - CRATER ARCUATE-LOBATE SCARPS. Lobate scarps inside some Upper Imbrian craters. *Interpretation:* materials of slumps/landslides formed by surface manifestation of listric faulting

pre-Nectarian Crater Materials

pNcu	pNcu - PEAK RING of highly degraded flat-floored craters
pNc	pNc - CRATER INTERIORS. Floor and inner terraced rim of highly degraded and flat-floored pre-Nectarian craters; interpreted as pre-Nectarian in age based on correlation of the absolute model ages and morphology
pNse	pNse - EJECTED MATERIAL. Highly degraded ejecta of the pre-Nectarian craters

Materials with Undifferentiated Age

sc	sc - SATELLITIC AND SECONDARY CRATERS. Clusters and chains of secondary craters of different ages excluding material of Orientale basin

Basin Materials

Ioc	Ioc - MATERIAL OF ORIENTALE-BASIN. Smooth light plains, clusters and chains of secondary craters that point toward the Orientale basin. *Interpretation:* Ejecta of the Orientale basin
SPA	SPA - SOUTH POLE-AITKEN MASSIFS. Isolated, high-standing massifs with steep slopes that lack overlapping ejecta. *Interpretation:* exposed remnants of the rim of the South Pole-Aitken basin
pNmb	pNmb - BASIN MATERIAL. Morphologically homogenous hummocky/rugged surfaces with fragments of rims of ancient impact structures. *Interpretation:* remnants of pre-Nectarian – Nectarian craters and basins

Plains Materials

Light Plains

lp	lp - LIGHT PLAINS. Light-toned, smooth and/or cratered plains that occur in craters and in the intercrater space, undifferentiated. *Interpretation:* deposits of finer-grain ejecta of remote craters and basins
Ilp2	Ilp2 – LIGHT PLAINS. Light-toned, smooth and/or cratered plains that occur in craters and in the intercrater space; interpreted as Upper Imbrian age based on correlation of the absolute model ages and morphology. *Interpretation:* deposits of finer-grain ejecta of remote craters and basins
Ilp1	Ilp1 – LIGHT PLAINS. Light-toned, smooth and/or cratered plains that occur in craters and in the intercrater space; interpreted as Lower Imbrian age based on correlation of the absolute model ages and morphology. *Interpretation:* deposits of finer-grain ejecta of remote craters and basins
Nlp	Nlp - LIGHT PLAINS. Light-toned, smooth and/or cratered plains that occur in craters and in the intercrater space; interpreted as pre-Nectarian - Nectarian age based on correlation of the absolute model ages and morphology. *Interpretation:* deposits of finer-grain ejecta of remote craters and basins

In Crater Dark Plains

Cmrp	Cmrp – IN CRATER LIGHT-TONED PLAINS. Morphologically rough plains on the floor of crater Schomberger A. *Interpretation:* impact melt materials
Imrp2	Imrp2 – IN CRATER LIGHT-TONED PLAINS. Morphologically rough plains on the floor of crater Hale; absolute model ages 3.68 +0.02/-0.023 Ga. *Interpretation:* impact melt materials
Imsp2	Imsp2 - IN CRATER LIGHT-TONED PLAINS. Morphologically smooth plains on the floor of crater Hale; absolute model ages 3.68 +0.02/-0.023 Ga. *Interpretation:* impact melt materials
Imrp1	Imrp1 - IN CRATER LIGHT-TONED PLAINS. Morphologically rough plains on the floor of crater Moretus; absolute model ages 3.75 +0.014/-0.015 Ga. *Interpretation:* impact melt materials
Imsp1	Imsp1 - IN CRATER LIGHT-TONED PLAINS. Morphologically smooth plains on the floor of crater Moretus; absolute model ages 3.75 +0.014/-0.015 Ga. *Interpretation:* impact melt materials
Nmrp	Nmrp - IN CRATER LIGHT-TONED PLAINS. Morphologically rough plains on the floor of large Nectarian craters. *Interpretation:* impact melt materials
Nmsp	Nmsp - IN CRATER LIGHT-TONED PLAINS. Morphologically smooth plains on the floor of large Nectarian craters. *Interpretation:* impact melt materials

Dark Plains

Ipx2	Ipx2 – DARK PLAINS. Dark mantling deposits with diffuse boundaries, sparsely-cratered and formed by smooth material, in spatial association with pits and graben in the Schrödinger basin; absolute model ages 3.72 +0.030/-0.038 Ga. *Interpretation:* deposits of mare pyroclastic materials
Ilv2	Ilv2 - DARK PLAINS. Smooth plains of darker tone with boundaries clearly seen deformed by wrinkle ridges, highlighted by elevated concentrations of FeO and high-Ca pyroxene in Kaguya data (Lemelin et al., 2022). Localized on the floor of Antoniadi crater; 3.46 +0.020/-0.023 Ga. *Interpretation:* plains formed by basaltic lava flows
Ilv1	Ilv1 - DARK PLAINS. Smooth plains of darker tone with boundaries clearly seen; deformed by wrinkle ridges, highlighted by elevated concentrations of FeO and high-Ca pyroxene in Kaguya data (Lemelin et al., 2022). Localized on the floor of Schrödinger basin; 3.84 +0.027/-0.033 Ga. *Interpretation:* plains formed by basaltic lava flows

Linear Structures, Point Features and Contacts

Linear Structures

gr	gr - GRABENS. System of linear groves. *Interpretation:* System of grabens possibly formed above magmatic dikes in Schrödinger basin, or due to intrusion and floor uplift. Floor in pre-Nectarian crater (356°E 82.8°S) and lower Imbrian Moretus craters also display grooves, but show no signs of volcanic activity
wr	gr - WRINKLE RIDGES. System of linear uplifted features. *Interpretation:* Tectonic forms caused by volcanic activity in Schrödinger basin
ls	ls - LOBATE SCARPS. Scarps, mapped in four localities; features less than ~35 km long. *Interpritation:* Tectonic scarps, possible evidence of young tectonic activity in the lunar crust

Point Features

●	SMALL CRATER. Small endogenic crater. *Interpretation:* Summit depression that is thought to be the source of pyroclastic mate rials (Schrödinger G)

Contacts

○	Solid contact line. Show certain border of the unit
◌	Dashed contact line. Show approximate border of the unit

6. Discussion

6.1. Topographic configuration of the studied region

The formation of the SPA basin was the main relief-forming event for the SCR. The map area overlays the southern edge of the SPA between 120–280ºE. Despite the topographically prominent rim of the basin, the overall topographic variations in the map area are characterized by a unimodal hypsogram (Fig. 1b). This result is unexpected because both the floor and ejecta domains of the SPA basin are separated by the rim crest of the basin, which constitute the majority of the map area (Fig. 1a). The unimodality of the hypsogram indicates that the regional scarp of the rim domain is not steep and contiguous enough to distinctly separate two different topographic levels of the floor and ejecta domains. In contrast, the topographic configuration of the opposite, northern edge of the SPA is characterized by a pronounced bimodality of the hypsogram (Ivanov et al., 2018b).

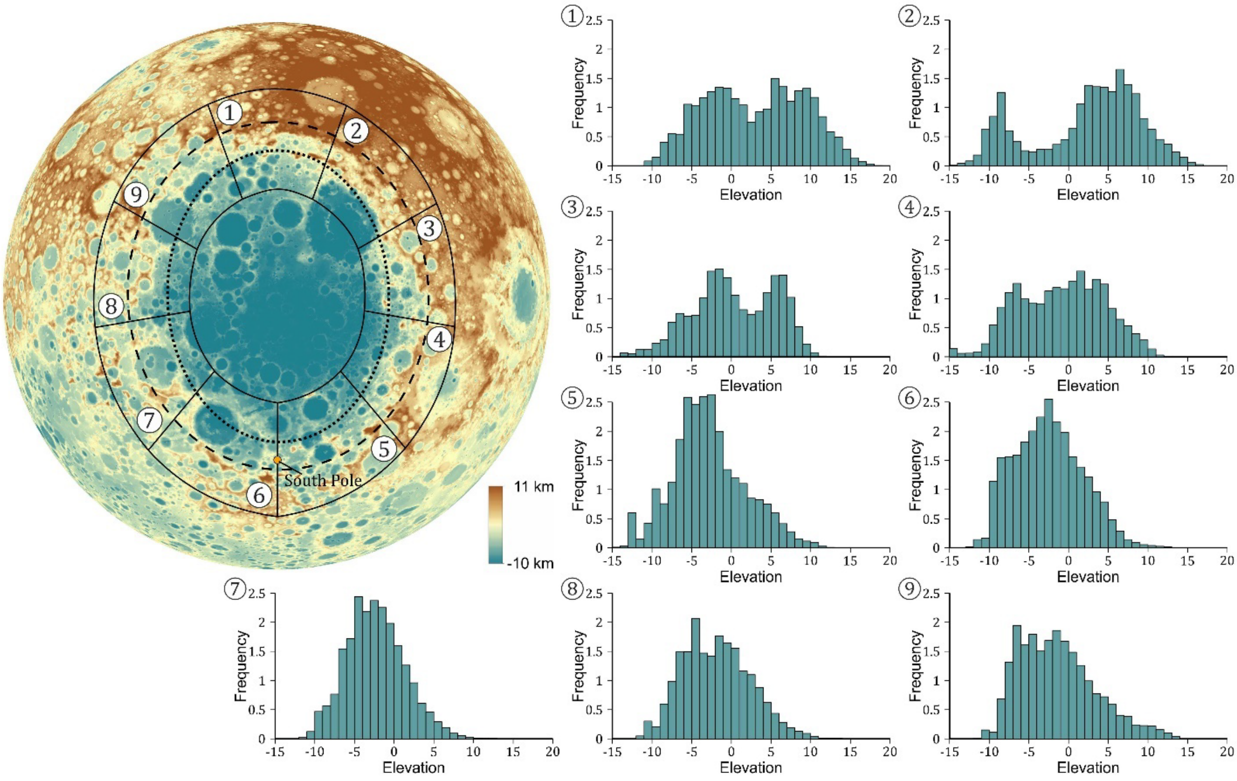

Fig. 14. Topographic configuration of the transitional zone from the floor of the SPA basin to its rim. Thin black lines show topographic samples; their numbers correspond to the numbers of histograms. Thick black lines, dotted and dashed, indicate the best fit and the outer ellipses respectively, from Garrick-Bethell and Zuber, (2009).

To characterize the distinct differences in the topographic configurations of the SPA at its transition from the floor to the rim, we have collected topographic data from the 1/64 degree/pix topographic map (resolution ~500 m/pix) at randomly selected points within large areas (2–4 x 10^5 km^2) that overlay the best fit ellipse and the outer ellipse defined by Garrick-Bethell and Zuber, (2009); the density of the points was the same in each area, one point per 200 km^2. The sets of collected topographic data were used to construct hypsograms that characterized different SPA segments. A unimodal hypsogram characterizes a gradual transition from the floor to the rim of the basin, whereas a bimodal hypsogram indicates the existence of two topographic levels (the floor and the rim) that are separated by a steep regional scarp. We prefer to use the hypsograms to characterize the general topographic characteristics of the SPA because individual topographic profiles have very complex shapes due to numerous impact structures that superpose the ancient SPA basin.

The results of our study are summarized in Fig. 14. The figure shows that the bimodal hypsograms occur only at the northeastern edges of the basin, in areas 1 and 2. The other hypsograms are essentially unimodal. These results suggest that only at the northeastern edge of the SPA basin does a sufficiently steep scarp exist that shows a distinction between the floor and the rim of the basin; in all other parts of the basin, this transition is gradual.

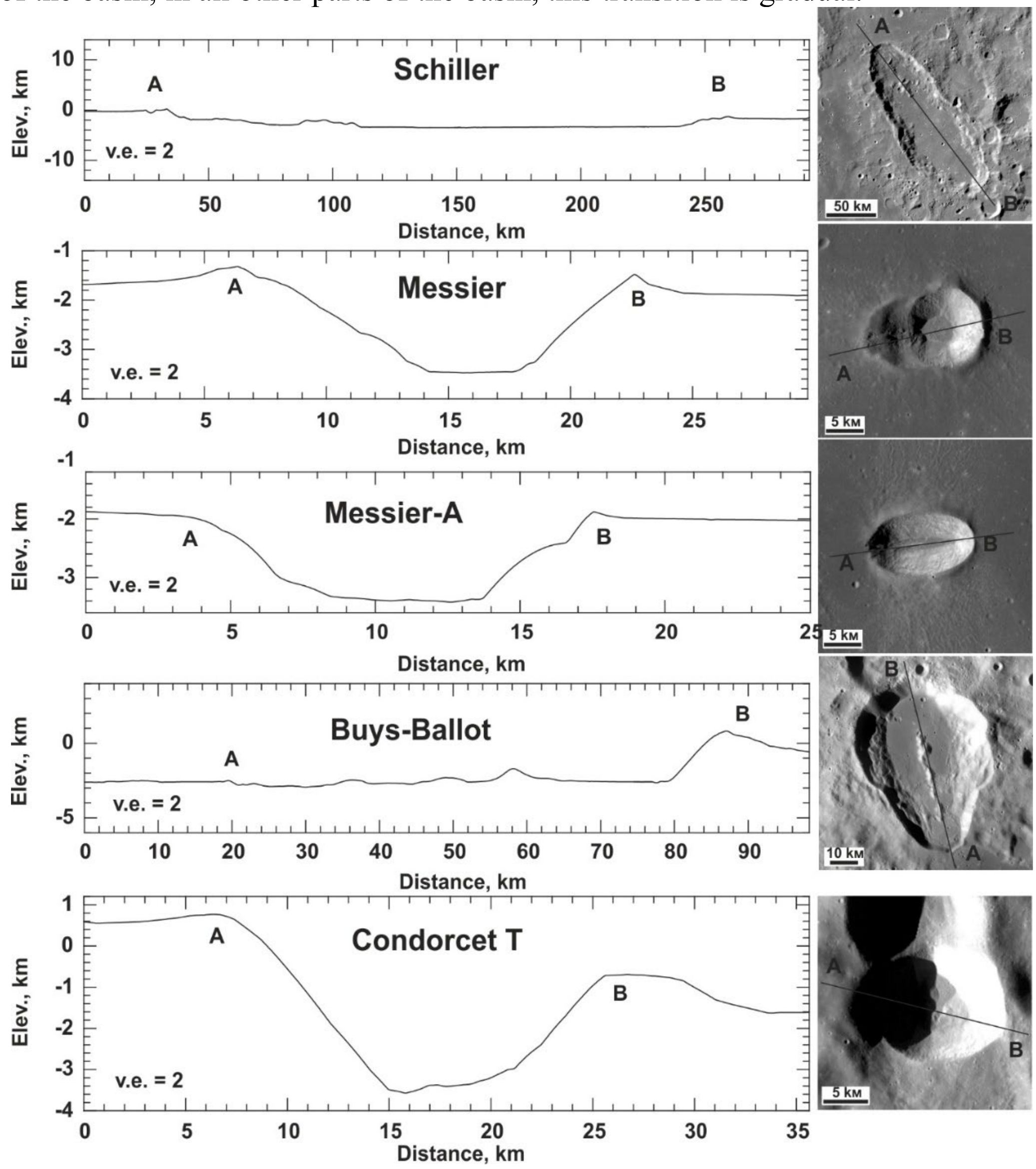

Fig. 15. Topographic profiles of the long axes of several oblique impact craters on the Moon. Topography from the LOLA topographic map, resolution 512 pix/deg. Steep sides of the profiles correspond to the uprange side of the craters.

Several reasons could have caused the asymmetric shape of the SPA basin. (1) The rim crest of the basin (except its northeastern portion) was degraded by the later impact events and/or viscous relaxation of the high topography (Solomon et al., 1982). (2) The rim crest of the basin (again, except its northeastern portion) was overlain by ejecta of younger basins (e.g., Orientale). (3) The topographic asymmetry is a possible consequence of the original topographic configuration of the basin due to its formation by an oblique impact. The formation of the SPA basin due to an oblique impact was first proposed by Schultz (1997) based on the topographic and gravimetric signatures of the basin and its generally elongated shape.

If the SPA is formed by a giant oblique impact, then a major question is related to the direction of the projectile trajectory, which is still unclear (Schultz, 1997, 2007; Garrick-Bethell and Zuber, 2009; Schultz and Crawford, 2011). Much smaller craters formed by oblique impact are characterized by pronounced asymmetry along the projectile trajectory with a steeper uprange wall and more gently sloping downrange wall (Gault and Wedekind, 1978) and the highly elongated craters on the Moon, which are thought to be formed by oblique impacts, reveal such a topographic asymmetry (Fig. 15). The existence of a pronounced regional scarp only at the northeastern edge of the SPA basin may suggest that this was an uprange side of the basin whereas the southern portion of the basin corresponds to the downrange side. Alternatively, the higher topography at the northern rim and the adjacent surroundings may be the result of ejecta due to an oblique impact in the direction from South to North (Garrick-Bethell and Zuber, 2009; Melosh et al., 2017; Moriarty et al., 2021).

6.2. Composition and surface properties of defined geological units

The portrayed spatial and temporal morphological units mapped in the SCR (Fig. 13) assists in addressing the problem of the mineralogical variations of the lunar crust in space and time. The data recently published by Lemelin et al., (2022) allow compositional assessment of units defined and mapped in the polar region.

Compositional variations seen in newly available data cubes (Lemelin et al., 2022) are correlated with the general topographic configuration of the map area, which was initially established by the SPA basin impact. M^3 data show elevated mafic and noritic mineralogical signatures mainly inside the best-fit (Fig. 1) topographic ellipse of SPA (Moriarty and Petro, 2020). The noritic anomaly is likely associated with material from the lower crust and upper mantle (Melosh et al., 2017; Moriarty et al., 2021). Based on Lunar Prospector data, thorium and iron minerals are also noticeable inside the best-fit topographic ellipse (Garrick-Bethell and Zuber, 2009). The SPA floor domain is noticeably poorer in plagioclase compared with the rim and ejecta domains (e.g., Moriarty and Pieters, 2018). Such a distribution suggests that the SPA impact redeposited plagioclase-richer materials and non-plagioclase lithologies were exposed on the basin floor. None of the post-SPA material units defined in our study correlate with the spatial distribution of plagioclase. We interpret this to mean that the post-SPA basin impacts could not homogenize the principal pattern of the plagioclase distribution created by the SPA event.

The map area shows a bimodal distribution of FeO. This component is noticeably more abundant within the SPA basin floor domain and emphasizes the well-known SPA iron anomaly (e.g. Lawrence et al., 2002), whereas the rim and potential zone of the ejecta of the basin are iron-poorer regions.

Within the floor domain, the most prominent high-FeO spots (Lemelin et al., 2022, their Fig. 5) corresponds to crater de Forest (~55 km diameter) and its ejecta, and smooth plains on the floor of Schrödinger basin. Although similar in terms of the high FeO-concentration, these localities are very different geologically (Whitten and Head, 2015). Smooth plains on the floor of the Schrödinger basin most likely represent basaltic lava flows (Kramer et al., 2013), which are expected to be iron-rich. In contrast, crater de Forest shows no signs of the presence of smooth, low-albedo (presumably basaltic) plains either inside the crater or in its ejecta. The unusually high FeO concentrations associated with the crater and lack of evidence of volcanic activity in the surface morphology and albedo suggest that the de Forest impact event has excavated FeO-rich materials from the subsurface.

Crater de Forest is characterized by enhanced FeO and high-calcium pyroxene signatures (Lemelin et al., 2022) that are characteristics of basaltic lava in the south polar region, e.g., mare spots in Mare Australe.

The FeO signature of de Forest could be either local (i.e., volcanic filling on the floor, or cryptomare, or intrusion(s)) or foreign (i.e., remnants of an iron projectile, or remote ejecta of higher-iron materials). The second (foreign) explanation appears unlikely: impact-forming projectiles do not remain intact, and there is no high-iron source area for the remote ejecta (the SPA floor has less iron than it is observed in the de Forest area). Thus, the local/volcanic explanation of the iron anomaly at the crater is more plausible than the alternative. Crater de Forest is within the SPA-floor domain and has no flat, smooth floor, which could indicate post-crater volcanic activity. On the other hand, de Forest is large enough, ~55 km across, to have excavated material from a significant depth, perhaps ~5 km; magmatic bodies could occur at this depth. These may also represent a more deeply-buried cryptomare that lost its morphological signature of the smooth plains. The problem with the cryptomare explanation for the de Forest iron anomaly is that it is the only crater in the broad surroundings that shows the enhanced iron signature (e.g., Whitten and Head, 2015). Morphologically, crater de Forest appears as a younger impact structure (it has a sharp rim and distinguishable terraced walls) than the more degraded neighboring craters de Forest N (40 km diameter, 70 km from de Forest), Brashear P (68 km diameter, 95 km from de Forest), and Brashear (60 km diameter, 125 km from de Forest). The location of these craters, their dimensions, apparently older age, and obvious absence of iron anomalies in association with them suggest that the enhanced FeO signature of de Forest either represents a very localized feature, or it formed after the formation of the iron-free large craters, or both. In any case, it is likely that the FeO anomaly at de Forest reflects the existence of localized magmatic body(s) that may or may not be related to the late evolution of the lunar magma ocean (e.g. Moriarty et al., 2021).

Floor-fractured craters that may indicate subsurface magmatic processes (Schultz, 1976) have not been detected within the map area except the Schrödinger basin (Jozwiak et al., 2012; Kramer et al., 2013). Two craters in the study region, Moretus (70.6ºS 354ºE, 114 km) and u one unnamed crater (82.8ºS 356.4ºE, 32 km), show one or two small graben on their floors but these craters do not fit all of the defining criteria for floor-fractured craters (Jozwiak et al., 2012). All larger craters (>100 km) in the map area (Table 1) have flat floors covered by plains-forming materials. Among these craters, only Schrödinger (133ºE, 74.7ºS, 313 km, SPA-ejecta domain) and Antoniadi (69.4ºS 187ºE, 137 km, SPA-floor domain) show noticeably elevated concentrations of both FeO and high-Ca pyroxene (Lemelin et al., 2022). One more crater, Casatus (72.8ºS 329ºE 103 km, SPA-ejecta domain), shows weaker enhancements of these basalt-indicative components. The scarcity of plains that have volcanic spectral signatures in each domain of the SPA in the map area suggests that the region around the South Pole (southward of 70ºS) was largely volcanically inactive since the formation and evolution of the SPA basin, but may host magmatic basalt dikes that did not reach the surface due to thicker farside crust (Head and Wilson, 2017), a possible explanation for the de Forest crater mafic anomaly.

Lunar regolith undergoes chemical and physical changes over time. The maturation of regolith (Morris, 1978) leads to its optical darkening. Lucey et al. (1995, 1998, 2000) developed the optical maturity parameter (OMAT) algorithm, which permits the estimation of the maturity of the surface. We used the results of the calibrated OMAT algorithm developed by Lemelin et al., (2022) to compare with our geological data. A map sector between ~150–210ºE shows a significant increase of the OMAT parameter value related to ejecta from Imbrian craters such as Antoniadi and de Forest. Eratosthenian craters Laveran and Hale Q, and Copernican craters Schomberger A, Schomberger J, and Schomberger L also show the presence of immature material. About 58 primary and secondary craters of these ages (from the small Eratosthenian craters in the Schrödinger basin to the Lower Imbrian crater Moretus) show the presence of fresher materials in their ejecta/interiors (see Table 1S in supplementary materia).

The data reported in Lemelin et al., (2022) show that the OMAT index is noticeably higher in a region southward of about 80ºS where materials of the Nectarian and pre-Nectarian ages dominate. This region corresponds to the transition from the floor to the rim domains of the SPA basin and is characterized by contrasting topography where slopes (at a baseline of 60 m) exceeding 20º prevail. The overall steepness of the relief in this region may have caused enhanced rejuvenation of the regolith by mass-wasting processes and, hence, an increase of the OMAT index. Another explanation of these anomalies may be related to the secondary craters and fine-grained ejecta that form rays of Shackleton and Tycho craters (Bernhardt et al., 2022).

6.3 Variations of the water equivalent hydrogen

One of the most intriguing characteristics of the lunar polar regions is enhanced concentrations of hydrogen in the regolith (Feldman et al., 1998, 2000, 2001; Mitrofanov et al., 2007, 2010; Boynton et al., 2012; Sanin et al., 2012, 2017), which can be expressed as model concentrations of water equivalent hydrogen (often interpreted as subsurface ice), WEH (Sanin et al., 2017) with resolution 3 km/pix. The WEH spatial distribution is highly variable, and its highest values occur at craters Cabeus (0.54±0.07 wt.%), Shoemaker (0.51±0.04 wt.%), Haworth (0.44±0.04 wt.%), Nobile (0.37±0.05 wt.%), de Gerlache (0.36±0.03 wt.%), Amundsen (0.34±0.08 wt.%) and Idel'son L (0.34±0.07 wt.%). The ages of these craters vary: Upper Imbrian (Idel'son L), Lower Imbrian (Shackleton), Nectarian (Amundsen and de Gerlache), pre-Nectarian (Faustini, Cabeus, Shoemaker, Haworth, Nobile).

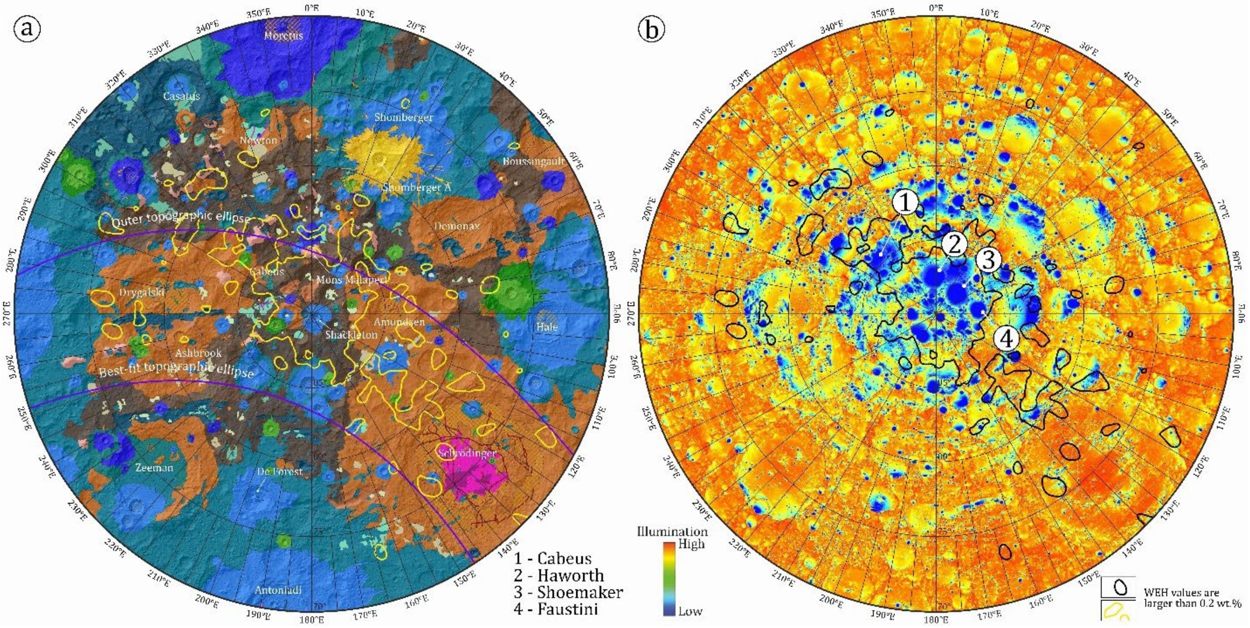

Fig. 16. The WEH anomalous regions (the WEH values are larger than 0.2 wt.%). a) The position of the anomalies (yellow lines) on the geological map. b) The position of the anomalies on the illumination map (illumination data are from Mazarico et al., (2011)).

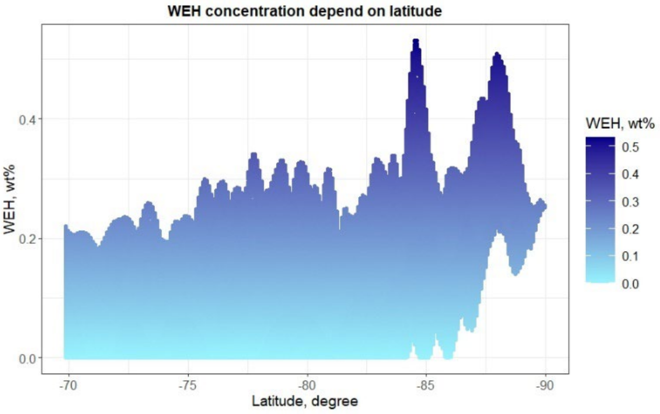

Fig. 17. WEH concentration depends on latitude (data from Sanin et al., 2017).

The mean value of the WEH in the map area is ~0.12±0.08 wt.%. Thus, we considered areas with WEH values above 0.2 wt.% as regions with an anomalous concentration of hydrogen in the regolith. Most of these regions are located in the rim domain of the SPA, where they are spatially associated with the pre-Nectarian and Nectarian units and preferentially occur in low-illuminated areas (Fig. 16). Floors of some craters are covered by permanently shadowed regions (PSRs) (Fig. 16, b) and almost all of them have significant increase of WEH distribution.

The spatial distribution of the WEH values shows no correlation with the regional geology and none of the time-stratigraphic units (except the Copernican System) is characterized by noticeable higher/lower values of the WEH. The mean WEH value for units of the Eratosthenian System is ~0.15±0.09 wt.%, Upper Imbrian Series is ~0.10±0.08 wt.%, Lower Imbrian Series is ~0.08±0.07 wt.%, Nectarian System is ~0.13±0.07 wt.%, and pre-Nectarian System is ~0.16±0.09 wt.%. The distinctly lower values for the Copernican materials (0.04±0.04 wt%) are likely to be due to the small total area of these units, 1.4% of the total map area (Tab. 2). The lack of correlation between the spatial distribution of the WEH values and regional stratigraphy and the tendency of concentration of the high-WEH spots at the lower-illuminated areas suggest that there are no specific substrate materials responsible for the variations of the WEH values. It is likely that hydrogen in the polar regolith is related to the environments favorable to the arrival and preservation of the solar wind protons at the lower-illuminated areas and the WEH variations may be formed relatively recently (e.g., during Eratosthenian or Copernican time). This conclusion is supported by a steady increase of the mean zonal WEH values from 70°S to the Pole (Fig. 17), independent of the regional stratigraphy.

6.4 Assessment of geology and stratigraphy of future targeted landing regions: The example of the Luna-25 mission

Here we present an example application of the SCR geologic map for the stratigraphic analysis of proposed landing sites of the Luna-25 mission. Geological mapping (Fig. 13) provides information about unit morphology, origin, stratigraphy and age, as well as the provenance of materials making up the surface. Combining this information with model thicknesses of ejecta of different ages allows reconstruction of the interior structure in the subsurface and assessment of the provenance of materials that can be analyzed at the landing sites. We applied this approach to the landing sector (Fig. 18a) of the Luna-25 mission (Krasilnikov et al., 2022). In our research, we used three models to understand the thicknesses of ejecta material: (1) Sharpton's (2014) formula was used for small craters (<45 km in diameter); (2) the Housen et al. (1983) model was used for craters more than 45 km in diameter; and (3) the Fassett et al. (2011) model was used for estimating ejecta thicknesses of basins.

It is possible to detect all large craters and basins that affect surface unit formation. For these impact structures, the absolute and/or relative age can be estimated. As a result, it is possible to construct geological cross-sections with the calculated model ejecta thicknesses that show the sub-surface stratigraphy and structure in the landing ellipse (Fig. 18c).

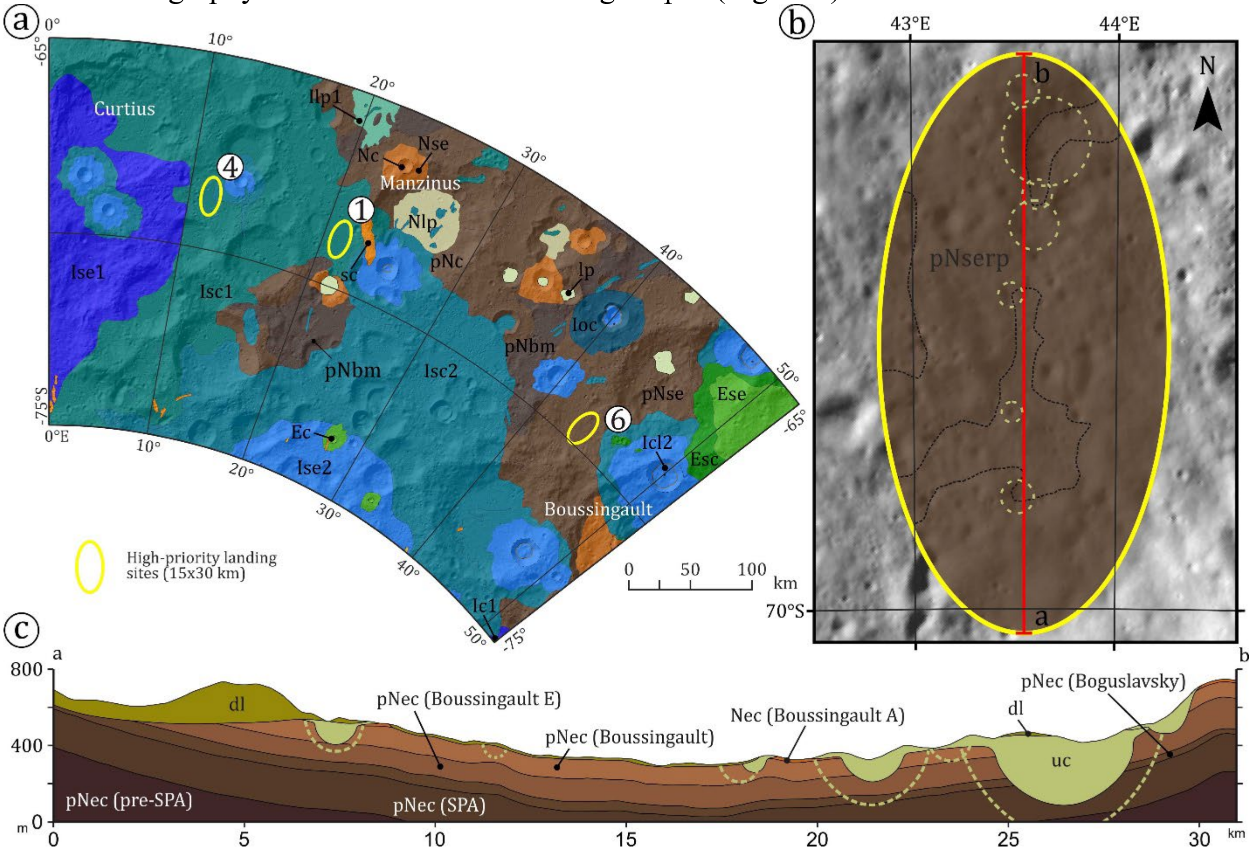

Fig. 18. (a) The Luna-25 landing sector with three main landing ellipses. (b) The geological structure of ellipse-6, the most probable landing site, at the local scale (1:100 000). rp – rolling plains with a low to medium density of craters; dark dotted line outlines elongated depressions; bright dotted circles show small craters that affect the layers shown in the cross-section (c) Geological cross-section showing our stratigraphic model of ellipse-6; calculated thickness of ejecta material described in text. dl – landslide material; uc – deposits of small craters with an actual size (dotted line).

Ellipse 1 (68.77° S, 21.21° E) is located on an intercrater plain formed by the ejecta of craters Manzinus and Simpelius A, interpreted to be of pre-Nectarian (pNec) age. The pre-SPA material ejecta from the SPA basin has an estimated thickness of about 870 m. The next layer is sourced from crater Manzinus (pre-Nectarian) with a thickness of 180 to 85 m from NE to SW, respectively. Above this layer, the Simpelius A (pNec) crater ejecta is 35–18 m thick from the SW to NE. The near-surface zone is represented by undifferentiated deposits of pre-Nectarian (Manzinus N, 6 to 1 m thickness, W-E; Manzinus D, 22–5 m, SE-NE), Nectarian (Manzinus S, 19–2 m, S-N) and Upper Imbrian (Manzinus E, 2–1 m, E-W) ages. Upper Imbrian deposits in this ellipse have a thickness from 7 to 6 m. The section is complicated by small craters, marked as uc. The excavation depth of all large craters, except for craters Manzinus H (pNec) and Manzinus E (UpImb), is greater than the thickness of the SPA ejecta, and their ejecta may contain material that comes from below the SPA basin ejecta deposit. Moretus crater is ~ 115 km in diameter and its approximate excavation depth is ~12 km. This impact event could have redeposited ancient, pre-SPA, materials overlain by the SPA deposit.

Ellipse 4 (68.65° S, 11.55° E) has the most complex geological and geomorphological structure. The ellipse is located on an intercrater plain composed of ejecta from craters Curtius, Simpelius E, and, presumably, Pentland A and Simpelius A of pre-Nectarian and Nectarian ages. Subsequently, the surface was covered by ejecta from the Lower Imbrian Moretus crater. A significant part of the ellipse is overlapped by ejecta from the Upper Imbrian crater Pentland E, located to the NE of the ellipse. The thickness of the SPA basin deposit is about 850 m. The northwestern part of the ellipse is complicated by the uneven thickness of ejecta from Curtius crater (pNec), with a variation in thickness from 90 to 52 m from NE to SW. Stratigraphically above this ejecta from pre-Nectarian craters Simpelius E (95–8 m thick, from S to N) and Simpelius A (48–21 m thick, from SE to NW). The upper layers in the eastern part of the ellipse may contain material from craters Simpelius H and Simpelius F. Material from crater Pentland A (Nec) formed ejecta 63–10 m thick decreasing in a NE-SW direction. The upper layer within the ellipse is composed of ejecta from the Lower Imbrian Moretus crater with a thickness of 7–6 m from SW to NE.

Ellipse 6 (69.55° S, 43.54° E) has a relatively homogeneous geological and geomorphological structure (Fig. 18b). The ellipse is located between three large pre-Nectarian craters: Boguslawsky (~95 km diameter), Boussingault (~128 km) and Boussingault E (~107 km). The surface of the ellipse is composed mainly of ejecta from crater Boussingault and possibly from the neighboring craters Boussingault A (Nec), Boussingault K, and Boussingault F (Ic2). At the base of the geological cross-section of ellipse 6 (Fig. 18a), pre-SPA materials are covered by SPA deposits with a thickness of about 1 km. These materials are overlain by ejecta from Boguslawsky crater, with a thickness of 74–32 m in the S-N direction. Stratigraphically above are deposits of the Boussingault E (pNec) (152–95 m, NE-SW) and Boussingault (pNec) (210–85 m, E-W) craters. Deposits of the Nectarian crater Boussingault A are discontinuous and have a thickness of 20–14 m. The thickness of deposits of the youngest large craters Boussingault F (UpImb) and Boussingault K (UpImb) inside the ellipse is less than 2 m and apparently did not have a significant influence on the geological structure of the region.

7. Conclusions

A combination of new remote sensing data – WAC mosaic (100 m/pix resolution), NAC images (~0.5–1 m/pix resolution) and the LOLA-derived DTMs with a resolution of 20–80 m/pix, spectral data and traditional geological mapping techniques (e.g., Wilhelms, 1972, 1987) enabled the compilation of a new geological map at 1:300 000 scale. We defined morphologically uniform units and traced their contacts using optical images and high-resolution altimetry data. In this way, we have defined and mapped the following material units: (1) high-standing massifs of the SPA basin, (2) crater-related units – walls, rims, and ejecta of impact craters and smaller basins, (3) plains units of both impact (impact melt and/or Cayley Formation) and volcanic origins (lava plains and pyroclastic deposits). In some places, these units are deformed by five types of structural features such as: (1) arcuate lobes from listric wall failure that occur in many bowl-shaped craters; (2) crater wall parallel step-like terraces that reflect degradation of their topography; (3) graben depressions and (4) wrinkle ridges that deform the surface of volcanic plains; (5) lobate scarps that occur in a few localities inside and outside of the crater interiors.

Mapping morphologically homogenous crater-related units permitted systematic determinations of the absolute model ages of about 200 craters using CSFD measurements on their floors and proximal ejecta deposits. In this way, we were able to calibrate observable morphology in terms of absolute model age and outline materials belonging to different periods of lunar geologic history at a higher level of confidence.

Because our mapping was partly based on topographic data, we investigated in detail the topographic configuration of the southern portion of the SPA basin, which characterizes about half of the map area. In contrast to its northern portion, where there are two distinct topographic levels (the floor and the rim) and the hypsogram is strongly bimodal (Ivanov et al., 2018b), the southern part of the basin is characterized by a unimodal hypsogram, which indicates the lack of a regional scarp separating different levels. Further investigation of the topography along the transition zone between the floor and the rim of the basin revealed that only its northern portion (between ~170°E and ~130°W) is characterized by topographic bimodality. The other portions of the zone show a gradual transition. Such a noticeable topographic asymmetry of the basin is consistent with its formation by an oblique impact (e.g., Schultz, 1997, 2007; Schultz and Crawford, 2011) in the direction from north to south.

Lunar Prospector data show thorium and iron anomaly within the best-fit topographic ellipse of the SPA basin (Garrick-Bethell and Zuber, 2009). In the same area, M^3 data shows elevated mafic abundance and a noritic lithology (Moriarty and Petro, 2020). The mapping of material units of different stratigraphic ages allows their direct comparison with new chemical and mineralogical interpretations of Kaguya data for the southern polar region (Lemelin et al., 2022). The higher concentrations of FeO and high-calcium pyroxene typical of basaltic magmatic/volcanic activity were found only in three localities: in the Schrödinger basin, on the floor of Antoniadi crater, and in the interior and ejecta of de Forest crater. In the first two cases, volcanic plains on the floor of the impact structures are responsible for the increase of FeO and high-calcium pyroxene. In the case of the de Forest crater, the higher FeO and HCP signatures are likely to be related to shallow intrusive bodies, possibly a dike. The scarcity of the signatures related to volcanic activity around the South Pole (southward of 70°S) suggests that this region was largely volcanically inactive subsequent to the formation and evolution of the SPA basin.

The OMAT parameter calculated by Lemelin et al. (2022) shows a noticeable increase for Imbrian and younger craters. This suggests that impact events as old as the Imbrian age still exert an influence on the texture and optical properties of the regolith. The increase of the OMAT parameter in association with the older, pre-Nectarian and Nectarian terrains occurs in places in the transition zone from the floor to the rim domains of the SPA basin. The increase of the OMAT parameter in these areas likely reflects enhanced mass-wasting processes in areas of steep topography.

Variations in the concentration of water equivalent hydrogen in the regolith within the map area suggest that WEH values higher than ~0.2 wt.% represent anomalous regions (mean + 3σ). Most of these regions are located within the SPA's rim domain, where they are associated with the pre-Nectarian and Nectarian units that dominate the rim region. However, the areas of anomalously high concentration of WEH values preferentially occur in low-illuminated areas and show a lack of correlation with variations of the local or regional geology. This suggests that none of the rock-stratigraphic units are responsible for the WEH anomalies, and the spatial distribution of hydrogen is mostly controlled by polar illumination conditions (permanent shadows), which is consistent with the increase of WEH values toward the South Pole.

Finally, the compiled geological map, in combination with the model estimates of the thickness of ejecta deposits of different ages, provides the opportunity to construct geological cross-sections. These represent snapshots of the 3D models of local to regional stratigraphy and can play an important role in the selection of potential landing sites for future missions (e.g., Luna-25 (e.g., Ivanov et al., 2018), Artemis (NASA, 2020), Chang'e-6), and in the assessment of the provenance of materials that compose the regolith at the landing sites.

Acknowledgments:

The work of SSK, MAI and ASK is partly supported by the Russian Science Foundation grant № 21-17-00035: Estimates of the rate of exogenous resurfacing on the Moon.

References

Baker, D.M.H., Head, J.W., Fassett, C.I., Kadish, S.J., Smith, D.E., Zuber, M.T., Neumann, G.A., 2011. The transition from complex crater to peak-ring basin on the Moon: New observations from the Lunar Orbiter Laser Altimeter (LOLA) instrument. Icarus 214, 377–393. https://doi.org/10.1016/J.ICARUS.2011.05.030

Barker, M.K., Mazarico, E., Neumann, G.A., Smith, D.E., Zuber, M.T., Head, J.W., 2021. Improved LOLA elevation maps for south pole landing sites: Error estimates and their impact on illumination conditions. Planet. Space Sci. 203, 105119. https://doi.org/10.1016/j.pss.2020.105119

Barker, M.K., Mazarico, E., Neumann, G.A., Zuber, M.T., Haruyama, J., Smith, D.E., 2016. A new lunar digital elevation model from the Lunar Orbiter Laser Altimeter and SELENE Terrain Camera. Icarus 273, 346–355. https://doi.org/10.1016/J.ICARUS.2015.07.039

Basilevsky, A.T., Krasilnikov, S.S., Ivanov, M.A., Malenkov, M.I., Michael, G.G., Liu, T., Head, J.W., Scott, D.R., L., L., Lark, L., 2019. Potential lunar base on Mons Malapert: topographic, geologic and trafficability considerations. Sol. Syst. Res. 53, 383–398. https://doi.org/10.1134/S0038094619050022

Bernhardt, H., Robinson, M.S., Boyd, A.K., 2022. Geomorphic map and science target identification on the Shackleton-de Gerlache ridge. Icarus, 379, 114963. https://doi.org/10.1016/j.icarus.2022.114963

Blewett, D.T., Lucey, P.G., Hawke, B.R., Jolliff, B.L., 1997. Clementine images of the lunar sample-return stations: Refinement of FeO and TiO_2 mapping techniques. J. Geophys. Res. Planets 102, 16319–16325. https://doi.org/10.1029/97JE01505

Boynton, W. V., Droege, G.F., Mitrofanov, I.G., McClanahan, T.P., Sanin, A.B., Litvak, M.L., Schaffner, M., Chin, G., Evans, L.G., Garvin, J.B., Harshman, K., Malakhov, A., Milikh, G., Sagdeev, R., Starr, R., 2012. High spatial resolution studies of epithermal neutron emission from the lunar poles: Constraints on hydrogen mobility. J. Geophys. Res. Planets 117, 0–33. https://doi.org/10.1029/2011JE003979

Deutsch, A.N., Heldmann, J.L., Colaprete, A., Cannon, K.M., Elphic, R.C., 2021. Analyzing Surface Ruggedness Inside and Outside of Ice Stability Zones at the Lunar Poles. Planet. Sci. J. 2, 213. https://doi.org/10.3847/PSJ/ac24ff

Dhingra, D., Head, J.W., Pieters, C.M., 2017. Geological mapping of impact melt deposits at lunar complex craters Jackson and Tycho: Morphologic and topographic diversity and relation to the cratering process. Icarus 283, 268–281. https://doi.org/10.1016/J.ICARUS.2016.05.004

Djachkova, M. V, Litvak, M.L., Mitrofanov, I.G., Sanin, A.B., 2017. Selection of Luna-25 landing sites in the South polar region of the Moon. Sol. Syst. Res. 51, 185–195. https://doi.org/10.1134/S0038094617030029

Fassett, C.I., Head, J.W., Smith, D.E., Zuber, M.T., Neumann, G.A., 2011. Thickness of proximal ejecta from the Orientale Basin from Lunar Orbiter Laser Altimeter (LOLA) data: Implications for multi-ring basin formation. Geophys. Res. Lett. 38, L17201. https://doi.org/10.1029/2011GL048502

Feldman, W.C., Lawrence, D.J., Elphic, R.C., Barraclough, B.L., Maurice, S., Genetay, I., Binder, A.B., 2000. Polar hydrogen deposits on the Moon. J. Geophys. Res. E Planets 105, 4175–4195.

https://doi.org/10.1029/1999JE001129

Feldman, W.C., Maurice, S., Binder, A.B., Barraclough, B.L., Elphic, R.C., Lawrence, D.J., 1998. Fluxes of fast and epithermal neutrons from lunar prospector: Evidence for water ice at the lunar poles. Science (80-.). 281, 1496–1500. https://doi.org/10.1126/science.281.5382.1496

Feldman, W.C., Maurice, S., Lawrence, D.J., Little, R.C., Lawson, S.L., Gasnault, O., Wiens, R.C., Barraclough, B.L., Elphic, R.C., Prettyman, T.H., Steinberg, J.T., Binder, A.B., 2001. Evidence for water ice near the lunar poles. J. Geophys. Res. E Planets 106, 23231–23251. https://doi.org/10.1029/2000JE001444

Fortezzo, C.M., Spudis, P.D., Harrel, S.L., 2020. Release of the digital unified global geologic map of the Moon at 1:5,000,000-scale. 51th Lunar and Planet. Sci. Conf. 2760.

Garrick-Bethell, I., Zuber, M.T., 2009. Elliptical structure of the lunar South Pole-Aitken basin. Icarus 204, 399–408. https://doi.org/10.1016/J.ICARUS.2009.05.032

Gault, D.E., Wedekind, J.A., 1978. Experimental studies of oblique impact. NASA 91, 399–404.

Guo, D., Liu, J., Head, J.W., Kreslavsky, M.A., 2018. Lunar Orientale impact basin secondary craters: spatial distribution, size-frequency distribution, and estimation of fragment size. J. Geophys. Res. Planets 123, 1344–1367. https://doi.org/10.1029/2017JE005446

Halliday, A.N., 2000. Terrestrial accretion rates and the origin of the Moon. Earth Planet. Sci. Lett. 176, 17–30. https://doi.org/10.1016/S0012-821X(99)00317-9

Head, J.W., 1975. Processes of lunar crater degradation: Changes in style with geologic time. moon 1975 123 12, 299–329. https://doi.org/10.1007/BF02629699

Head, J.W., 1974. Orientale multi-ringed basin interior and implications for the petrogenesis of lunar highland samples. Moon 11, 327–356. https://doi.org/10.1007/BF00589168

Head, J.W., Pieters, C., McCord, T., Adams, J., Zisk, S., 1978. Definition and detailed characterization of Lunar surface units using remote observations. Icarus 33, 145–172. https://doi.org/10.1016/0019-1035(78)90030-1

Head, J.W., Wilson, L., 2017. Generation, ascent and eruption of magma on the Moon: New insights into source depths, magma supply, intrusions and effusive/explosive eruptions (Part 2: Predicted emplacement processes and observations). Icarus 283, 176–223. https://doi.org/10.1016/J.ICARUS.2016.05.031

Hiesinger, H., van der Bogert, C.H., Pasckert, J.H., Schmedemann, N., Robinson, M.S.S., Jolliff, B., Petro, N., 2012. New crater size-frequency distribution measurements of the South Pole-Aitken Basin. 43th Lunar and Planet. Sci. Conf. 2863, 2.

Housen, K.R., Schmidt, R.M., Holsapple, K.A., 1983. Crater ejecta scaling laws: fundamental forms based on dimensional analysis. J. Geophys. Res. 88, 2485–2499.

Ivanov, B.A., Stöffler, D., 2005. The Steinheim impact crater, Germany: Modeling of a complex crater with central uplift. 36th Lunar Planet. Sci. Conf. 1443.

Ivanov, M. A., Abdrakhimov, A. M., Basilevsky, A. T., Demidov, N. E., Guseva, E. N., Head, J. W., Hiesinger, H., Kohanov, A.A., Krasilnikov, S.S., 2018a. Geological characterization of the three high-priority landing sites for the Luna-Glob mission. Planetary and Space Science, 162, 190-206. https://doi.org/10.1016/j.pss.2017.08.004

Ivanov, M.A., Hiesinger, H., van der Bogert, C.H., Orgel, C., Pasckert, J.H., Head, J.W., 2018b. Geologic history of the northern portion of the South Pole-Aitken basin on the Moon. J. Geophys. Res. Planets 123, 2585–2612. https://doi.org/10.1029/2018JE005590

Jozwiak, L.M., Head, J.W., Zuber, M.T., Smith, D.E., Neumann, G.A., 2012. Lunar floor-fractured craters: Classification, distribution, origin and implications for magmatism and shallow crustal structure. J. Geophys. Res. Planets 117, 11005. https://doi.org/10.1029/2012JE004134

Kirk, R.L., Archinal, B.A., Gaddis, L.R., Rosiek, M.R., 2008. Cartography for Lunar exploration: 2008 status and mission plans. Int. Arch. Photogramm. Remote Sens. Spat. Inf. Sci. XXXVII, 1473–1490.

Kramer, G.Y., Kring, D.A., Nahm, A.L., Pieters, C.M., 2013. Spectral and photogeologic mapping of Schrödinger Basin and implications for post-South Pole-Aitken impact deep subsurface stratigraphy. Icarus 223, 131–148. https://doi.org/10.1016/j.icarus.2012.11.008

Krasilnikov, A.S., Krasilnikov, S.S., Ivanov, M.A.A., Head, J.W., 2023. Estimation of ejecta thickness from impact craters in the South polar region of the Moon. Sol. Syst. Res. 57. (in press)

Krasilnikov, S.S., Krasilnikov, A.S., Ivanov, M.A., 2022. Geological details of the main landing ellipses of Luna-25. Sol. Syst. Res. 56, 135–144. https://doi.org/10.1134/S0038094622020058

Lawrence, D.J., Feldman, W.C., Elphic, R.C., Little, R.C., Prettyman, T.H., Maurice, S., Lucey, P.G., Binder, A.B., 2002. Iron abundances on the lunar surface as measured by the Lunar Prospector gamma-ray and neutron spectrometers. J. Geophys. Res. Planets 107, 13–1. https://doi.org/10.1029/2001JE001530

Lee, D.C., Halliday, A.N., Snyder, G.A., Taylor, L.A., 1997. Age and origin of the Moon. Science (80-.). 278, 1098–1103. https://doi.org/10.1126/science.278.5340.1098

Lemelin, M., Lucey, P.G., Camon, A., 2022. Compositional analysis of the Moon in the visible and near-infrared regions. Planet. Sci. J. 3, 63. https://doi.org/10.3847/PSJ/ac532c

Li, S., Lucey, P.G., Milliken, R.E., Hayne, P.O., Fisher, E., Williams, J.-P., Hurley, D.M., Elphic, R.C., 2018. Direct evidence of surface exposed water ice in the lunar polar regions. Proc. Natl. Acad. Sci. U. S. A. 115, 8907–8912. https://doi.org/10.1073/pnas.1802345115

Litvak, M.L., Mitrofanov, I.G., Sanin, A.B., Golovin, D. V., Malakhov, A. V., Boynton, W. V., Droege, G.F., Harshman, K., Starr, R.D., Milikh, G., Sagdeev, R., 2012. LEND neutron data processing for the mapping of the Moon. J. Geophys. Res. Planets 117, n/a-n/a. https://doi.org/10.1029/2011JE004035

Lu, Y., Wu, Y., Michael, G.G., Basilevsky, A.T., Li, C., 2019. Young wrinkle ridges in Mare Imbrium: Evidence for very recent compressional tectonism. Icarus 329, 24–33. https://doi.org/10.1016/j.icarus.2019.03.029

Lucchitta, B.K., 1978. Geologic map of the north side of the Moon (I-1062). USGS. https://doi.org/10.3133/I1062

Lucey, P.G., Blewett, D.T., Hawke, B.R., 1998. Mapping the FeO and TiO_2 content of the lunar surface with multispectral imagery. J. Geophys. Res. Planets 103, 3679–3699. https://doi.org/10.1029/97JE03019

Lucey, P.G., Blewett, D.T., Jolliff, B.L., 2000. Lunar iron and titanium abundance algorithms based on final processing of Clementine ultraviolet-visible images. J. Geophys. Res. Planets 105, 20297–20305. https://doi.org/10.1029/1999JE001117

Lucey, P.G., Jeffrey Taylor, G., Malaret, E., 1995. Abundance and distribution of iron on the Moon. Science (80-.). 268, 1150–1153. https://doi.org/10.1126/SCIENCE.268.5214.1150

Lucey, P.G., Spudis, P.D., Zuber, M., Smith, D., Malaret, E., 1994. Topographic-compositional units on the moon and the early evolution of the lunar crust. Science (80-.). 266, 1855–1858. https://doi.org/10.1126/SCIENCE.266.5192.1855

Mazarico, E., Neumann, G.A., Smith, D.E., Zuber, M.T., Torrence, M.H., 2011. Illumination conditions of the lunar polar regions using LOLA topography. Icarus 211, 1066–1081. https://doi.org/10.1016/J.ICARUS.2010.10.030

Melosh, H.J., 1989. Impact cratering : a geologic process. New York. Oxford Univ. Press 253 p.

Melosh, H.J., Kendall, J., Horgan, B., Johnson, B.C., Bowling, T., Lucey, P.G., Taylor, G.J., 2017. South Pole-Aitken basin ejecta reveal the Moon's upper mantle. Geology, 45(12), 1063-1066.

Meyer, H.M., Denevi, B.W., Boyd, A.K., Robinson, M.S., 2016. The distribution and origin of lunar light plains around Orientale basin. Icarus 273, 135–145. https://doi.org/10.1016/j.icarus.2016.02.014

Mishra, A., Kumar, P.S., 2022. Spatial and temporal distribution of lobate scarps in the Lunar South polar region: evidence for latitudinal variation of scarp geometry, kinematics and formation ages, neo-tectonic activity and sources of potential seismic risks at the Artemis candidate. Geophys. Res. Lett. 49, e2022GL098505. https://doi.org/10.1029/2022GL098505

Mitrofanov, I.G., Litvak, M.L., Sanin, A., Malakhov, A., Golovin, D., Boynton, W., Droege, G., Chin, G., Evans, L., Harshman, K., Fedosov, F., Garvin, J., Kozyrev, A., McClanahan, T., Milikh, G., Mokrousov, M., Starr, R., Sagdeev, R., Shevchenko, V., Shvetsov, V., Tret'yakov, V., Trombka, J., Varenikov, A., Vostrukhin, A., 2012. Testing polar spots of water-rich permafrost on the Moon: LEND observations onboard LRO. J. Geophys. Res. Planets 117, 14. https://doi.org/10.1029/2011JE003956

Mitrofanov, I.G., Sanin, A.B., Boynton, W. V., Chin, G., Garvin, J.B., Golovin, D., Evans, L.G., Harshman, K., Kozyrev, A.S., Litvak, M.L., Malakhov, A., Mazarico, E., McClanahan, T., Milikh, G., Mokrousov, M., Nandikotkur, G., Neumann, G.A., Nuzhdin, I., Sagdeev, R., Shevchenko, V., Shvetsov, V., Smith, D.E., Starr, R., Tretyakov, V.I., Trombka, J., Usikov, D., Varenikov, A., Vostrukhin, A., Zuber, M.T., 2010. Hydrogen mapping of the lunar south pole using the LRO neutron detector experiment LEND. Science (80-.). 330, 483–486. https://doi.org/10.1126/science.1185696

Mitrofanov, I.G., Zuber, M.T., Litvak, M.L., Demidov, N.E., Sanin, A.B., Boynton, W. V., Gilichinsky, D.A., Hamara, D., Kozyrev, A.S., Saunders, R.D., Smith, D.E., Tretyakov, V.I., 2007. Water ice permafrost on Mars : Layering structure and subsurface distribution according to HEND / Odyssey and MOLA / MGS data. Geophys. Res. Lett. 34, 1–5. https://doi.org/10.1029/2007GL030030

Moriarty, D.P., Petro, N.E., 2020. Mineralogical Diversity of the Lunar South Pole: Critical Context for Future Sample Return Goals and Interpretation. 51th Lunar and Planet. Sci. Conf. 2326.

Moriarty, D. P., Watkins, R. N., Valencia, S. N., Kendall, J. D., Evans, A. J., Dygert, N., & Petro, N. E. (2021). Evidence for a Stratified Upper Mantle Preserved Within the South Pole-Aitken Basin. Journal of Geophysical Research: Planets, 126(1), e2020JE006589. https://doi.org/10.1029/2020JE006589

Moriarty, D.P., Pieters, C.M., 2018. The character of South Pole-Aitken basin: patterns of surface and subsurface composition. J. Geophys. Res. Planets 123, 729–747. https://doi.org/10.1002/2017JE005364

Morris, R.V., 1978. The surface exposure (maturity) of lunar soils: Some concepts and IS/FeO compilation. 9th Lunar Planet. Sci. Conf. 2287–2297.

Muehlberger, W.R., Batson, R.M., Cernan, E.A., Freeman, V.L., Hait, M.H., Holt, H.E., Howard, K.A., Jackson, E.D., Larson, K.B., Reed, V.S., Rennilson, J.J., Schmitt, H.H., Scott, D.R., Sutton, R.L., Stuart-Alexander, D., Swann, G.A., Trask, N.J., Ulrich, G.E., Wilshire, H.G., Wolfe, E.W., 1973. Preliminary geologic investigation of the Apollo 17 landing site. Apollo 17 Prelim. Sci. Rep.

NASA, 2020. NASA's Plan for Sustained Lunar Exploration and Development. https://www.nasa.gov/sites/default/files/atoms/files/a_sustained_lunar_presence_nspc_report4220final.pdf

Neukum, G., Ivanov, B.A., Hartmann, W.K., 2001. Cratering records in the inner Solar system in relation to the Lunar reference system, in: chronology and evolution of Mars. Springer, Dordrecht, pp. 55–

86. https://doi.org/10.1007/978-94-017-1035-0_3

Neumann, G.A., Zuber, M.T., Wieczorek, M.A., Head, J.W., Baker, D.M.H., Solomon, S.C., Smith, D.E., Lemoine, F.G., Mazarico, E., Sabaka, T.J., Goossens, S.J., Melosh, H.J., Phillips, R.J., Asmar, S.W., Konopliv, A.S., Williams, J.G., Sori, M.M., Soderblom, J.M., Miljkovic, K., Andrews-Hanna, J.C., Nimmo, F., Kiefer, W.S., 2015. Planetary Science: Lunar impact basins revealed by gravity recovery and interior laboratory measurements. Sci. Adv. 1. https://doi.org/10.1126/SCIADV.1500852/SUPPL_FILE/1500852_SM.PDF

Oberbeck, V.R., 1975. The role of ballistic erosion and sedimentation in lunar stratigraphy. Rev. Geophys. 13, 337–362. https://doi.org/10.1029/RG013I002P00337

Ohtake, M., Haruyama, J., Matsunaga, T., Yokota, Y., Morota, T., Honda, C., Team, L., 2008. Performance and scientific objectives of the SELENE (KAGUYA) Multiband Imager. Earth Planets Sp. 60, 257–264.

Petro, N.E., Pieters, C.M., 2006. The Effects of Basin Formation on the Lunar Geochemical Terranes. 37th Lunar and Planet. Sci. Conf. 1868.

Petro, N.E., Pieters, C.M., 2004. Surviving the heavy bombardment: ancient material at the surface of South Pole-Aitken basin. J. Geophys. Res. Planets 109, 6004. https://doi.org/10.1029/2003JE002182

Pieters, C.M., Staid, M.I., Fischer, E.M., Tompkins, S., He, G., 1994. A sharper view of impact craters from Clementine data. Science (80-.). 266, 1844–1848. https://doi.org/10.1126/science.266.5192.1844

Pike, R.J., 1977. Apparent depth/apparent diameter relation for lunar craters. Proc. Lunar Sci. Conf. 8th 3427–3436.

Pike, R.J., 1976. Crater dimensions from apollo data and supplemental sources. The Moon. 153 15, 463–477. https://doi.org/10.1007/BF00562253

Poehler, C.M., Ivanov, M.A., Bogert, C.H. Van Der, Hiesinger, H., Pasckert, J.H., Wright, J., Head, J.W., 2020. The lunar South Pole-Aitken basin region: a new geological map. EPSC2020 14, 19–21.

Robinson, M.S., Brylow, S.M., Tschimmel, M., Humm, D., Lawrence, S.J., Thomas, P.C., Denevi, B.W., Denevi, P.. ., Bowman-Cisneros, E., Zerr, J., Ravine, M.A., Caplinger, M.A., Ghaemi, F.T., Schaffner, J.A., Malin, M.C., Mahanti, P., Bartels, A., Anderson, J., Tran, T.N., Eliason, E.M., McEwen, A.S., Turtle, E., Jolliff, B.L., Hiesinger, H., 2010. Lunar Reconnaissance Orbiter Camera (LROC) instrument overview. Space Sci. Rev. 150, 81–124. https://doi.org/10.1007/s11214-010-9634-2

Sanin, A.B., Mitrofanov, I.G., Litvak, M.L., Bakhtin, B.N., Bodnarik, J.G., Boynton, W. V., Chin, G., Evans, L.G., Harshman, K., Fedosov, F., Golovin, D. V., Kozyrev, A.S., Livengood, T.A., Malakhov, A. V., McClanahan, T.P., Mokrousov, M.I., Starr, R.D., Sagdeev, R.Z., Tret'yakov, V.I., Vostrukhin, A.A., 2017. Hydrogen distribution in the lunar polar regions. Icarus 283, 20–30. https://doi.org/10.1016/j.icarus.2016.06.002

Sanin, A.B., Mitrofanov, I.G., Litvak, M.L., Malakhov, A., Boynton, W. V., Chin, G., Droege, G., Evans, L.G., Garvin, J., Golovin, D. V., Harshman, K., McClanahan, T.P., Mokrousov, M.I., Mazarico, E., Milikh, G., Neumann, G., Sagdeev, R., Smith, D.E., Starr, R.D., Zuber, M.T., 2012. Testing lunar permanently shadowed regions for water ice: LEND results from LRO. J. Geophys. Res. Planets 117. https://doi.org/10.1029/2011JE003971

Schultz, P.H., 2007. A possible link between Procellarum and the South-Pole-Aitken basin. 38th Lunar and Planet. Sci. Conf. 1839, 2.

Schultz, P.H., 1997. Forming the South-Pole Aitken basin - the extreme games. 28th Lunar Planet. Sci. Conf., 1259–1260.

Schultz, P.H., 1978. Martian intrusions: possible sites and implications. Geophys. Res. Lett. 5, 457–460.

https://doi.org/10.1029/GL005I006P00457

Schultz, P.H., 1977. Endogenic modification of impact craters on Mercury. Phys. Earth Planet. Inter. 15, 202–219. https://doi.org/10.1016/0031-9201(77)90032-2

Schultz, P.H., 1976. Floor-fractured lunar craters. The Moon., 241–273. https://doi.org/10.1007/BF00562240

Schultz, P.H., Crawford, D., 2011. Origin of nearside structural and geochemical anomalies on the Moon in: Recent Advances and Current Research Issues in Lunar Stratigraphy, Ambrose, W. ed. Geological Society of America Special Paper.

Sharpton, V.L., 2014. Outcrops on lunar crater rims: Implications for rim construction mechanisms, ejecta volumes and excavation depths. J. Geophys. Res. E Planets 119, 154–168. https://doi.org/10.1002/2013JE004523

Shoemaker, E.M., Hackman, R.J., 1962. Stratigraphic basis for a lunar time scale, In: The Moon, Kopal, Zdenek, and Mikhailov, Z.K., eds., - Intern. Astronom. Union Symposium 14, Leningrad 1960, in: The Moon. Academic Press, New York, pp. 289–300.

Smith, D.E., Zuber, M.T., Jackson, G.B., Cavanaugh, J.F., Neumann, G.A., Riris, H., Xiaoli, S., Ronald, S.Z., Zellar, S., Coltharp, C., Connelly, J., Katz, R.B., Kleyner, I., Liiva, P., Matuszeski, A., Mazarico, E.M., McGarry, J.F., Novo-Gradac, A.-M., Ott, M.N., Peters, C., Ramos-Izquierdo, L.A., Ramsey, L., Rowlands, D.D., Schmidt, S., Stanley, V.S.I., Shaw, G.B., Smith, J.C., Swinski, J.-P., Torrence, M.H., Unger, G., Yu, A.W., Zagwodzki, T.W., 2010. The Lunar Orbiter Laser Altimeter investigation on the Lunar Reconnaissance Orbiter Mission. Sp. Sci Rev 150, 209–241. https://doi.org/10.1007/s11214-009-9512-y

Solomon, S.C., Comer, R.P., Head, J.W., 1982. The evolution of impact basins: Viscous relaxation of topographic relief. J. Geophys. Res. Solid Earth 87, 3975–3992. https://doi.org/10.1029/JB087IB05P03975

Spudis, P.D., 1993. The geology of multi-ring impact basins: the Moon and other planets. Cambridge: Cambridge University Press. https://doi.org/10.1017/CBO9780511564581

Stöffler, D., Ryder, G., 2001. Stratigraphy and isotope ages of lunar geologic units: chronological standard for the inner Solar system, in: Composition and origin of cometary materials. pp. 7–52.

Stöffler, D., Ryder, G., Ivanov, B.A., Artemieva, N.A., Cintala, M.J., Grieve, R.A.F., 2006. Cratering history and lunar chrnology. Rev. Mineral. Geochemistry. https://doi.org/10.2138/rmg.2006.60.05

Stuart-Alexander, D.E., 1978. Geologic map of the central far side of the Moon. USGS Map I-1047.

van der Bogert, C.H., Hiesinger, H., Dundas, C.M., Krüger, T., McEwen, A.S., Zanetti, M., Robinson, M.S., 2017. Origin of discrepancies between crater size-frequency distributions of coeval lunar geologic units via target property contrasts. Icarus 298, 49–63. https://doi.org/10.1016/J.ICARUS.2016.11.040

Walsh, J.M., Bailey, A.M., Bernhardt, H., Boyd, A.K., Wagner, R.V., Henriksen, M.R., M. S. Robinson, 2022a. Identification and Applications of South Pole-Aitken Basin Massifs. Annual Meeting of Planet. Geol. Map. p. 7046.

Walsh, J.M., Bailey, A.M., Wagner, R.V., Henriksen, M.R., Bernhardt, H., Boyd, A.K., Robinson, M.S., 2022b. Refining South Pole-Aitken Basin Ring Structure Using Gravimetry at Massifs. 53th Lunar and Planet. Sci. Conf. 2859.

Watters, T.R., Robinson, M.S., Collins, G.C., Banks, M.E., Daud, K., Williams, N.R., Selvans, M.M., 2015. Global thrust faulting on the Moon and the influence of tidal stresses. Geology 43, 851–854. https://doi.org/10.1130/G37120.1

Whitten, J., Head, J.W., Staid, M., Pieters, C.M., Mustard, J., Clark, R., Nettles, J., Klima, R.L., Taylor, L.,

2011. Lunar mare deposits associated with the Orientale impact basin: New insights into mineralogy, history, mode of emplacement, and relation to Orientale Basin evolution from Moon Mineralogy Mapper (M3) data from Chandrayaan-1. J. Geophys. Res. Planets 116, 0–09. https://doi.org/10.1029/2010JE003736

Whitten, J.L., Head, J.W., 2015. Lunar cryptomaria: Physical characteristics, distribution, and implications for ancient volcanism. Icarus 247, 150–171. https://doi.org/10.1016/J.ICARUS.2014.09.031

Wilhelms, D.E., 1987. The geologic history of the Moon. USGS Numbered Ser. Prof. Pap. 1348, 302 p. https://doi.org/10.3133/PP1348

Wilhelms, D.E., 1974. Interagency report: astrogeology 55, geologic mapping of the second planet. Part 1: Rationale and general methods of lunar geologic mapping. Part 2: Technicalities of map conventions, format, production mechanics, and reviewing. Part 3: History of the US. NASA. Ames Res. Cent. A Prim. Lunar Geol. (EE N75-13730 04-91) 199–238.

Wilhelms, D.E., 1972. Geologic mapping of the second planet. US Geol. Surv. Interag. Report, Astrogeology 55, 199–238.

Wilhelms, D.E., El-Baz, F., 1977. Geologic map of the East side of the Moon (Map I-948). USGS.

Wilhelms, D.E., Howard, K.A., Wilshire, H.G., 1979. Geologic map of the South side of the Moon. USGS Map I-1162.

Wilhelms, D.E., Mccauley, J.F., 1971. Geologic map of the near side of the Moon (Map I-703). USGS.

Wilson, L., Head, J.W., 2018. Lunar floor-fractured craters: Modes of dike and sill emplacement and implications of gas production and intrusion cooling on surface morphology and structure. Icarus 305, 105–122. https://doi.org/10.1016/J.ICARUS.2017.12.030